Additive Manufacturing 76 (2023) 103751

Contents lists available at ScienceDirect

Additive Manufacturing

journal homepage: www.elsevier.com/locate/addma

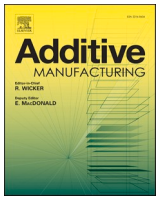

Experimental evaluation of hybrid lattice structures subjected to blast loading

Henrique Ramos [a,*], Erik Pickering [b,c], Sara AlMahri [a], Kapil Krishnan [a], Jide Oyebanji [a], Zhongwei Guan [a], Genevieve Langdon [b], Rafael Santiago [a]

[a] Advanced Materials Research Center, Technology Innovation Institute, Abu Dhabi, United Arab Emirates
[b] Department of Civil and Structural Engineering, University of Sheffield, Sheffield, UK
[c] Cranfield Forensics Institute, Cranfield University, Defence Academy of the United Kingdom, Shrivenham, UK

ARTICLE INFO

Keywords:
Lattice structures
Blast resistance
Additive manufacturing
High strain-rate loading
Design of experiments

ABSTRACT

Lattice structures have shown potential for efficient protection against dynamic loading events, especially during high-strain rate scenarios such as a blast. Additive manufacturing enables the design of complex geometries to optimise lattice architecture and increase blast resistance. However, the lack of experimental data related to blast-resistant lattice structures poses challenges in developing and validating theoretical and numerical models. This study aims to design blast-resistant lattice structures that can improve protection efficiency at wider applicability in high-strain rate loadings. For that, hybrid-layered Triply Periodic Minimal Surfaces (TPMS) lattice structures were systematically designed using a Design of Experiments (DoE) approach and manufactured using additive manufacturing (AM). The Blast Hopkinson Pressure Bar (BHPB) rig was used to compare the influence of different lattice topologies and relative densities on energy absorption when specimens were subjected to compressive blast loading. High-speed imaging was utilised to measure transient deformation in addition to the load transferred through the specimens. The experimental results indicated that the BHPB rig could appropriately measure the energy absorption of compressive structures subjected to shockwave loading. Additionally, the results demonstrated that TPMS topology and relative density changes substantially affect its performance. The DoE approach was utilised to predict the performance improvements of layered-hybrid lattice structures, providing valuable data for blast protection specialists and engineers designing AM lattice structures to resist blast loading.

1. Introduction

Innovative materials and manufacturing technologies offer enormous potential for enhancing the protective efficiency of blast and impact-resistant components. Accurate predictions of the structural response of such systems require an in-depth understanding of materials and structures when subjected to high strain rates and shockwave loading. Additionally, investigating components subjected to blast loading brings the opportunity to develop the sacrificial cladding capable of withstanding such hazardous conditions potentially applicable to aerospace, defence, and infrastructures.

Crushable materials, such as metallic foams and honeycombs, are used as cores in sandwich panels that form impact-resistant sacrificial claddings [1–9]. These assemblies can exhibit high blast-absorbing capabilities and weight reduction compared to equivalent monolithic panels [3]. However, the advent of additive manufacturing (AM) techniques allows the manufacturing of complex geometries (e.g., lattice structures) that can further enhance the impact energy absorption capability in cladding systems [10–17].

Lattice structures are complex topologies that can only be manufactured appropriately by AM. In recent studies, lattice structures have demonstrated outstanding potential for impact applications, including blast-resistant cladding [4,10,18–27]. Ramos et al. [28] reported the data obtained from high-rate compression and impact experiments, demonstrating that minor modifications to the gyroid lattice architectures substantially changed the impact response. Besides using functionally graded topologies, combining different topologies has also brought attention to energy absorption applications, i.e., lattice hybridisation. AlQaydi et al. [29] studied 18 combinations of Primitive and Schoen I-graph-wrapped package (IWP) topologies, pointing out

* Corresponding author.
E-mail address: Henrique.Ramos@tii.ae (H. Ramos).

https://doi.org/10.1016/j.addma.2023.103751
Received 6 April 2023; Received in revised form 1 August 2023; Accepted 20 August 2023
Available online 22 August 2023

that hybrid lattices can provide intermediate mechanical behaviour, which is useful for tailoring the lattice deformation and failure modes. Novak et al. [30] performed a similar study for various combinations of Gyroid and Diamond cells, showing that the failure mode initiates from the less stiff lattice topology.

Blast events involve the compression of gases with substantial kinetic energy and dynamic pressure, leading to hydrodynamic waves that reflect and diffract when encountering obstacles [31]. Given the dynamic impulse associated with blast events, solid materials are ill-equipped to withstand blast loads, which struggle to propagate the impulse across the cladding [32]. Conversely, lattice structures have exhibited their capacity to absorb energy through their deformable three-dimensional surfaces, as evidenced by numerous studies [32–36]. These findings have opened up vast possibilities for optimising and tailoring the mechanical and impact performance of structural components.

Smith et al. [27] were one of the first to study the blast response of AM lattice structures using SLM 316 L lattice-based. Their results demonstrated that the lattice structure's energy absorption characteristics and collapse mode exhibit a linear dependency on the applied impulse up to the threshold for material densification. McKown et al. [18] also investigated 316 L stainless steel SLM truss lattice structures, studying the absorbed energy and deformation modes through blast tests undertaken on a ballistic pendulum. A progressive buckling collapse was observed during the shock compression, while parametric studies indicated that the blast resistance of the lattice structures increased with increasing yield stress and was related to the structure specific energy absorption (SEA) characteristics. Using an explosive-driven shock tube, Stanczak et al. [1] conducted an experimental shock wave test on auxetic lattice structures. These tests were performed with explosive charges up to 70 g of equivalent trinitrotoluene (TNT), reaching overpressures up to 130 bar, which limited the study to low blast energies and low relative density lattices. Imbalzano et al. [37] conducted a numerical investigation on auxetic lattice structure sandwich panels subjected to localised impact from a projectile velocity of up to 200 m/s. Their findings highlight substantial reductions in back facet displacements (i.e., up to 56%) and plastic deformation of the auxetic core panels, demonstrating an enhanced localised impact resistance. These findings highlight the suitability of lattice structures in extreme applications, where materials and structures were subjected to high strains and strain-rates, like helmet protective padding and armored panels. The promising applications of lattices subjected to blast loadings require further investigations given the current paucity of information, experimental setup complexity, cost, restrictions, and risk.

Peng and Tran [38,39] used numerical models to explore Triply Periodic Minimal Surfaces (TPMS) lattices subjected to impulsive loading. Explicit finite element (FE) was employed to study the energy absorption of blast-loaded sandwich panels with gyroid lattice cores. Parametric studies suggested that functionally graded lattices could improve blast resistance. However, FE models were validated using quasi-static compression data, and no experimental blast tests were performed. Novak et al. [40] performed similar tests on Diamond, Gyroid, IWP, and Primitive TPMS lattices that illustrated the superior performance of functionally graded lattices, with a 25% enhancement of the energy absorption compared to strut-based lattices. In the same study, the authors conducted computational simulations to evaluate the blast behaviour of sandwich panels with TPMS cores. However, the predictions were validated against the dynamic compressive test data through which the Design of Experiments (DoE) did not adequately capture shockwave or explosion loading. Critchley et al. [41] also studied auxetic lattices made by AM by using a non-explosive shock tube, which also limited the study to a low shock-wave loading. Wei et al. [42] investigated the response of Ti–6Al–4 V auxetic honeycomb sandwich panels under blast loading conditions. Their study involved experimental study and numerical modelling of the deformation and failure behaviour caused by shockwave loading. The investigation highlights the enhanced blast resistance of AM auxetic honeycomb cores sandwich panels. However, evaluating energy absorption capabilities was solely conducted through the validated computational models.

Even though experimentally validated numerical models have been extensively used to predict the mechanical response of lattice structures, literature still needs to fully cover the design of lattice structures to satisfy defined requirements. DoE is a method used to estimate the values for the independent variables of a physical experiment or computer simulation with a specific objective, i.e., as the generation of a response-surface model of the phenomenon under investigation, represented as the dependent variable [43,44]. This response surface finds the optimal set of parameters that satisfies the objective function by generating a response surface from a group of variables and determining the optimal parameters. Thus, the use of DoE allows a systematic design of complex architectures of lattices and, to the best of the authors' knowledge, has not been reported in the literature, e.g., the design of sacrificial cladding for absorbing blast energy.

High-velocity detonation presents high levels of pressure loading [45–47]. Such dynamic event risks compromising structural integrity and facilitating the ingress of waves and explosion products into vehicles or structures. Even without rupture, dynamic pressure can induce fragmentation on the interior wall, threatening the occupants [32]. Many authors have also explored an alternative way to explosive detonations by using, for example, larger shock tube facilities [48], the Taylor test [49,50], Split Hopkinson Pressure Bar (SHPB) [51–53], or modified devices based on the Hopkinson technique [10,19,54–56].

The use of equivalent loading techniques is fundamentally motivated by the challenge of instrumenting near-field blast loading experiments, especially for high-strength materials loaded to failure. Whilst Hopkinson bar techniques have been used to accurately characterise the intense temporal and spatial pressure loading resulting from a near-field blast [57,58], the resultant fireball and detonation products [59,60] would obscure the visualisation of both the lattice topology response [28] and any boundary condition effects [61]. Despite the efforts, there is still a gap in terms of the mechanical evaluation of the blast performance of lattice structures. In most cases, the devices can provide equivalent impact energies and strain rates but do not replicate the same boundary conditions observed in real blast events, where a better approach to analyse the energy absorption capabilities of complex structures is urgently required.

In order to address these limitations, this study adopts the DoE methodology to systematically design hybrid-layered TPMS lattices, considering their topology and relative density, for enhancing SEA values of the hybrid lattices under blast loading conditions. Different combinations of lattice topologies (e.g., Gyroid, Diamond, Primitive, and IWP) and relative densities were proposed. Furthermore, an experimental blast rig device is designed to accurately measure near-field energy absorption in shockwave loading applicable to lattice structures. The resulting compressive response, SEA, impulse levels, and deformation mode were compared for all the lattice topologies tested.

2. Materials and methods

2.1. Hybrid lattice design

The TPMS-based lattice unit cells used in this study are shown in Fig. 1(a)–(d). TPMS topologies are described by the following mathematical surfaces [62].

$$\phi(x,y,z)_{gyroid} = \sin X\cos Y + \sin Y\cos Z + \sin Z\cos X \quad (1)$$

$$\phi(x,y,z)_{Diamond} = \cos X\cos Y\cos Z - \sin X\sin Y\sin Z \quad (2)$$

$$\phi(x,y,z)_{Primitive} = \cos X + \cos Y + \cos Z \quad (3)$$

$$\phi(x,y,z)_{Neovius} = 3(\cos X + \cos Y + \cos Z) + 4\cos X\cos Y\cos Z, \quad (4)$$

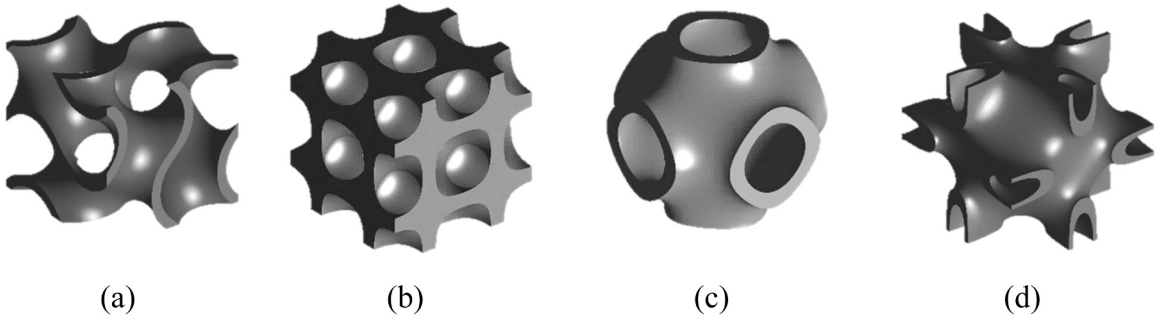

Fig. 1. TPMS unit cells and lattices designed: (a) Gyroid, (b) Diamond, (c) Primitive, and (d) Neovius.

where $X = 2\alpha\pi x$, $Y = 2\beta\pi y$, and $Z = 2\gamma\pi z$ control the unit size in the x-, y-, and z-directions, for $\alpha = \beta = \gamma = 1$ and $\phi = 0$. Relative densities ($\bar{\rho} = \rho_{Lattice}/\rho_{Solid}$) ranging from 20% to 40% were replicating configurations that best compromise for additively manufacture based on the experimental impact test developed previously [10].

For the DoE analysis, FE modelling was used to study the influence of relative density and lattice topologies variables on the blast loading response. Fig. 2a shows the model configuration, where TPMS lattice type variables are categorised by varying their lattice structure architectures, e.g., Gyroid, Diamond, Primitive, Neovius.

2.2. Design of experiments

Design of experiments (DoE) is generally adopted to minimise the

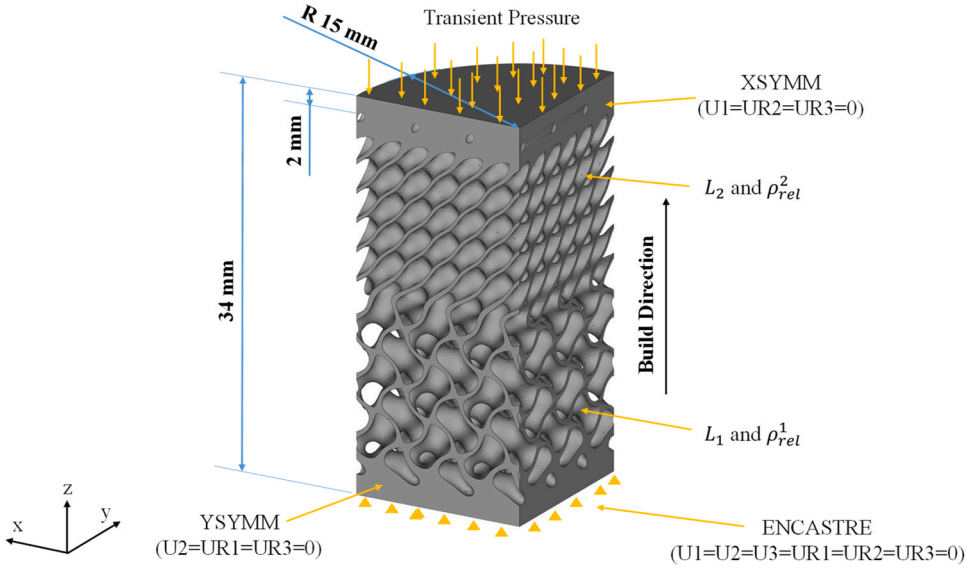

Fig. 2. (a) Quarterly symmetric FE model of a hybrid-layered lattice with described boundary constraints used in the DoE study and (b) schematic of lattice structures with build orientation within the build chamber.

number of experiments required to obtain optimal design or solutions. The principles of DoE can be applied to FE simulations to generate a response surface of the phenomenon under investigation and determine the design variables' influence on the response. Response surface methodology (RSM) comprises regression fitting to obtain approximate responses based on a sequence of DoE to obtain an optimal variable response [63]. The design variables for the DoE study are described in Table 1.

The lattice layer variables are categorical, with four TPMS lattice architectures (Gyroid, Diamond, Primitive, Neovius) as possible options. The relative density variables are numeric, with 0.2 (20% relative density) as the lower bound and 0.4 (40% relative density) as the upper bound. The measured response from the finite element simulations is the energy absorbed per unit mass of the specimen (SEA).

A second-order model is a specific type of polynomial regression model used in RSM. It includes linear, quadratic, and interaction terms to capture both linear and nonlinear effects of the input variables on the response variable and was selected to generate the mathematical model to represent the design variables [63], which is expressed as,

$$\varphi = \beta_0 + \sum_{j=1}^{k} \beta_j x_j + \sum_{j=1}^{k} \beta_{jj} x_j^2 2 + \sum_{i<j} \sum_{j=2}^{k} \beta_{ij} x_i x_j + \epsilon \tag{5}$$

where β_0 is the coefficient representing the mean of responses from all experiments, β_j is the coefficient for the effect of the variable on the response, and β_{ij} is the coefficient for the interaction of variables. These models are multiple linear regression models with k regressor variables. The second-order model allows for the definition of quadratic effects ($\beta_{jj}x_j^2$) and interaction effects ($\beta_{ij}x_i x_j$), in addition to the linear effects ($\beta_j x_j$), suitable for complex non-linear phenomena. Thus, the second-order model was adopted to identify numerical model parameters and predict the hybrid lattice structures' response under blast loadings. Finally, if the total number of experiments is n, the response surface can be expressed using matrix form, $Y = X\beta + \epsilon$ [63].

The DoE study uses the D-Optimal design methods to obtain the optimal lattice configurations and their respective relative densities. The influence of these variables on the response, such as SEA, is evaluated. For the D-Optimal design, a moment matrix is defined as.

$M = \frac{X^T X}{k}$. The D-Optimal design selects candidate points for experiments to maximise the determinant of the moment matrix. Usually, the D-Efficiency (D_{eff}) parameter is adopted as an index to judge the D-Optimality. D_{eff} is expressed as $D_{eff} = \frac{|M|^{1/p}}{k}$, where $p = k + 1$, when all the variables are normalised between − 1 and 1. The responses are then categorised in a normalised *desirability*, where 1 represents the D_{eff} response [63].

The D-Optimal design criteria generated a total of 42 runs to be performed in order to fit the response surface. Then an optimisation technique is used to determine the optimal values of the design variables that predict the overall simulation results with the least error. The candidate points for the D-Optimal design and the measured responses from the FE simulations are shown in Appendix.

Design-Expert software (StatEase, U.S.) was used to generate the configurations and analyse the RSM response, where different configurations of lattice were proposed based on the isosurface Eqs. (1)–(4) and relative density. The 3D computer-aided design (CAD) models of the hybrid-layered geometries were created in nTopology (nTopology, U.S.) software. The topologies were designed at different relative densities, achieved by varying the wall thickness in the software. Fig. 2a showcases a quarter CAD model of a cylindrical lattice manufactured using AM. The cylindrical blast samples have a diameter of ⌀ 30 mm and a height of 34 mm, with two lattice layers assembled between 2 mm thick plates. All lattice topologies comprise unit cells with a uniform size of 5 mm, with powder entrapment not being evidenced. FE mesh was generated was conducted by using the same software. The lattice model was preprocessed using a User MATerial (UMAT) subroutine, where final boundary conditions and transient pressure were applied. The FE analysis was carried out using Abaqus/explicit code (Dassault Systèmes, France), where material properties were collected from the authors' previous work [64,65]. Here, 10-noded tetrahedral elements C3D10M were employed to mesh the lattice with second-order formulations and hourglass control. A transient pressure load, obtained from experimental evaluation, is applied to the top surface, where the boundary conditions and symmetry constraints of the lattice model are shown in Fig. 2a. The design variables for the DoE study presented the lattice-type position and relative density, ρ_{rel}^i, in the i lattice type position. The hybrid lattice was designed with a 2 mm thickness plate on both edges from pressure loading distribution along the lattice cells. The proposed relative density gradients and lattice topologies were finally analysed using Design-Expert (StatEase, U.S.) software. Specific energy absorption (SEA) related to blast impact behaviour is defined as:

$$\text{SEA} = \frac{EA}{m} = \frac{1}{m}\int F d\delta \tag{6}$$

where F is compressive force, δ is the lattice displacement, m is the lattice mass, and EA is the energy absorbed, given by the area under the load-displacement curve. The experimental blast methodology is

Table 1
Design variables utilised in the DoE study.

Design Variable	Source
Type of *Layer 1*	L_1
Type of *Layer 2*	L_2
Relative density of *Layer 1*	ρ_{rel}^1
Relative density of *Layer 2*	ρ_{rel}^2

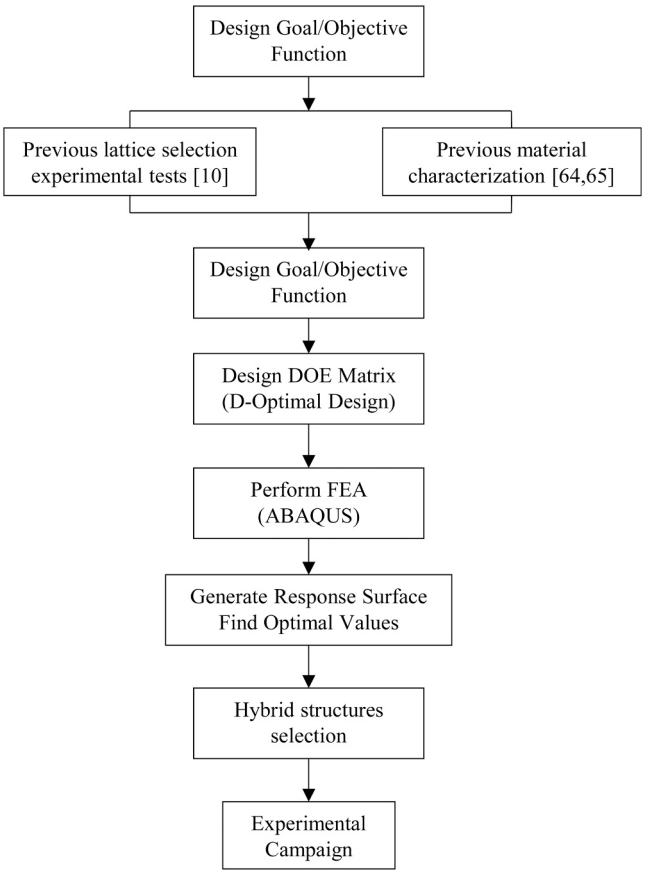

Fig. 3. Flow chart of the methodology used for the experimental blast campaign.

summarised in the flowchart in Fig. 3.

2.3. Additive manufacturing of hybrid lattice

The hybrid TPMS lattice samples were manufactured by the Laser Powder-Bed Fusion (L-PBF) technique using an EOS4 Concept Laser M1 (EOS, Germany) machine, the lattice structures schematic diagram with build orientation within the build chamber can be seen in Fig. 2b. The chemical compositions and manufacturing parameters are summarised in Tables 2 and 3, respectively. Previous studies have highlighted the significant contribution of the heat treatment process in mitigating the thermal stress induced by the temperature gradient during manufacturing L-PBF samples [10,65,66]. Therefore, a post-heat treatment cycle was conducted on all specimens using a vacuum furnace at 600 °C for 2 h, followed by furnace cooling.

Using metallographic procedures, porosity measurements were conducted where samples were collected from a lattice structure, cross-sectioned and polished [67,68]. The porosity was quantified by imaging processing in an Olympus DSX 1000 optical microscope-OM (Olympus, Japan). Porosity measurements were carried out using Olympus Stream Imaging Analysis software (Olympus, Japan) on the exposed cross-sectional surface of the sample, identifying the ROI (Region of Interest) along with the percentage of the sample surface density of the pores. To evaluate the surface quality, as-built lattices were imaged using a ThermoFisher model Scios 2 (Thermo Fisher Scientific, US) scanning electron microscope (SEM) with a secondary electron detector at an operating voltage of 5 keV.

2.4. Experimental setup

2.4.1. Test rig design

The specimens were all tested using the same test setup and loading conditions, as shown schematically in Fig. 4a. The rig is designed to enable high-speed imaging of the specimen deformation by transferring the blast load to the specimen via an EN24T steel anvil. The anvil transfers the load to the specimen, with the resulting axial strain history being transmitted into the EN24T steel bar mounted coaxially behind the specimen. The anvil is press-fit into the disposable PTFE gaskets to prevent the detonation products from obfuscating the camera footage of the specimens. In addition to the gaskets, the shroud plate and rig superstructure prevent the detonation flash, combustion product, and shock waves from obfuscating the camera footage.

The blast loading is applied by a centre detonated 30 g PE10 spherical explosive charge. The explosive is located within a disposable S355J2H steel blast tube, with the centre of the explosive located 120 mm from the face of the anvil. The blast tube is held in place by two press-fit disposable PLA tube grips such that the tube is placed flush against the anvil and gasket holders. The Euronel in-hole 500 ms non-electric detonator is fixed using a small disposable PLA detonator holder to locate the charge relative to the blast tube accurately. A PLA spall guard is installed to catch any spall of the PTFE gasket that occurs through the minor clearance gap between the anvil and the shroud plate. The combined use of spherical charges, blast tubes, and detonator locators enabled a highly repeatable blast loading, with a total impulse transfer of 32.62 ± 0.92 Ns, i.e., a standard deviation of only 2.8%.

2.4.2. Data processing

The Ø 49 mm Blast Hopkinson Pressure Bar (BHPB) is gauged at 750 mm from the loaded face in a half-bridge configuration with the gauges opposed to removing any potential bending effects. The data is captured at 5 MHz, triggered by a break-wire attached around the detonator adjacent to the explosive charge. A Photron Fastcam SA-Z type 2100 high-speed camera was used to monitor the specimen deformation at a frame rate of 252,000 frames per second. The specimen is front-lit by a Luminys 30 kW Linear LabLight, with an additional high-intensity continuous output LED backlight placed behind the specimen to improve edge contrast on the specimen. Photron FASTCAM Analysis (PFA) tracking system was used to measure the displacement evolution, where the correlation between the bars was used to measure the strain deformation response. The photography of the overall assembly can be seen in Fig. 4b.

A spectrogram using short-time Fourier transform (STFT) spectrum analysis was conducted to filter out higher frequencies noise levels by using a low-pass filter [69,70]. The experimental data were extracted, and STFT was computed by time segments given a spectral density. Fig. 5a presents the STFP spectrogram for the blast setup where it was possible to evaluate that the frequency spectrum of the strain signal varied throughout the test, and significant frequency components ranged until 50 kHz along the recorded spectrum. Then, a high-frequency spectrum filtering is conducted in the strain signals with a low-pass filter at a cut-off frequency of 50 kHz. A representative comparison curve of stress-strain is plotted in Fig. 5b, along with a corresponding filtered and non-filtered recorded response, where the two curves overlay, indicating a non-global change in the specimen's overall stress-time response.

In this study, a uniform blast loading was applied on the front face of the anvil. The deformation of the specimen, Δl, together with the stress response, $\sigma(t)$, is given by the following equations:

$$\Delta l = u_1 - u_2 \tag{7}$$

$$\sigma(t) = E_B \frac{A_B}{A_s} \varepsilon_t(t) \tag{8}$$

where u_1 and u_2 are the displacements of the impacted lattice sample obtained from high-speed camera images, and $\varepsilon_t(t)$ is the strain data recorded from the strain gauges on the transmitted bar. E_B is the elastic modulus of the transmitted bar, while A_B and A_s are the cross-sectional areas of the bar and the specimen, respectively.

A polynomial interpolation was used to resample the displacement uniformly in a fixed-rate data frequency as a physical triggering was used to synchronise the images and strain gauge data. For quantitative comparison, the impulse is also calculated based on the force resulting measurement in the transmitted bar being defined by the equation,

$$I = \int_0^\infty F(t)dt \tag{9}$$

where $F(t)$ is the force measured in the transmitted bar.

Table 3
L-PBF manufacturing parameters used.

Laser source	180 W, ytterbium fiber, single
Focus diameter	100μm
Chamber environment	Inert gas (nitrogen)
Particle size	10–45μm
Layer thickness	45 μm
EOS method (scanning strategy)	Continuous
Hatch spacing	0.15 mm
Laser speed	800 mm/s

Table 2
Chemical compositions of stainless steel SS316L alloy.

Component	Cr	Ni	Mo	Mn	Si	P	C	S	Fe
wt (%)	16–18	10–13	2.0–2.5	0–2	0–1.0	0–0.04	0–0.03	0–0.03	Balance

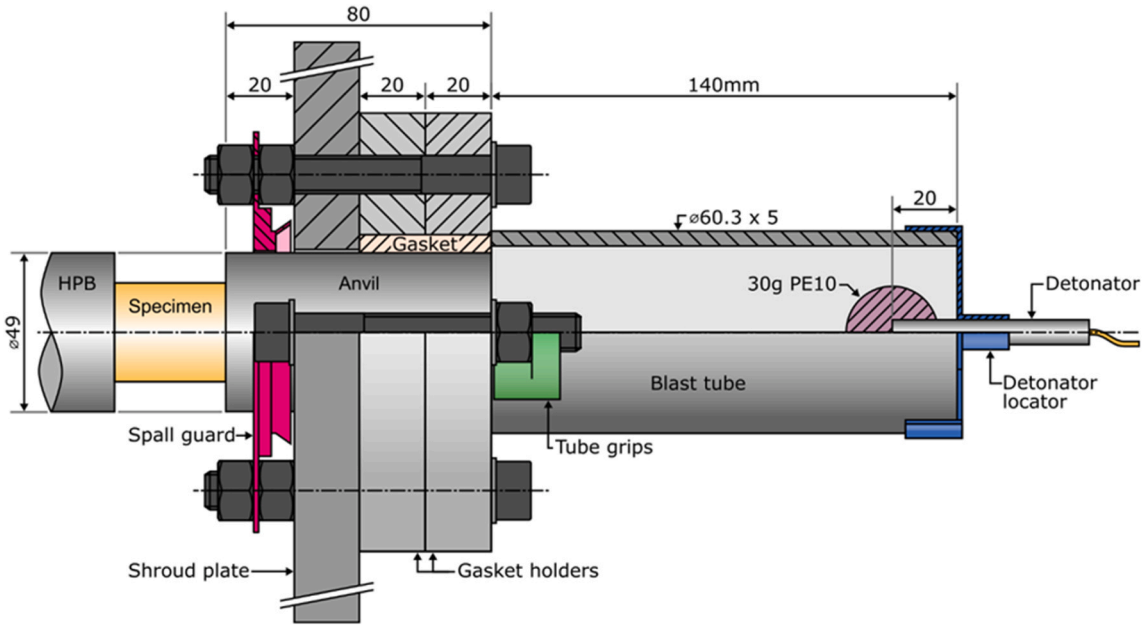

(a)

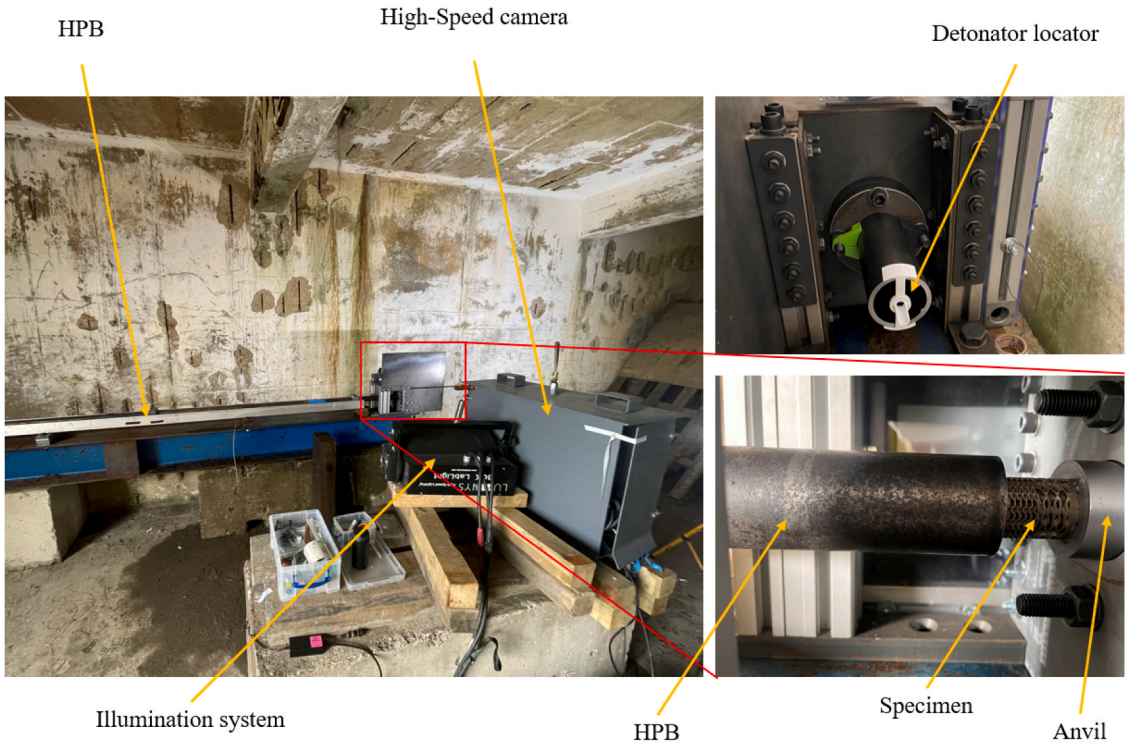

(b)

Fig. 4. (a) A partially sectioned schematic view of the experimental setup showing the PE10 explosive location inside the blast tube relative to the Blast Hopkinson Pressure Bar (BHPB), lattice specimen, and anvil. The PTFE gasket, PLA tube grips, and PLA detonator locator are replaced in each test. The high-speed camera and front light are aligned perpendicular to the page, and (b) the overall view with detailed information of the blast setup in the BPHB.

3. Results and discussion

3.1. Microstructural analysis

Porosity measurements were conducted to analyse the quality of AM samples, where measurements of pores of the control samples show that the specimens present an average porosity of 0.37% ± 0.06. The internal defects primarily consist of small spherical pores with a maximum average pore size of 0.12 ± 0.02 mm. These voids, as described by Zhang et al. [71], can result from the entrapment of gases within the melt pool due to a rapid cooling rate. Surface voids, as observed by scanning electron microscopy (Fig. 6b - d), are typically referred to as enclosed voids beneath the printed surface, where these incomplete fusion defects occur when there is insufficient input energy, resulting in

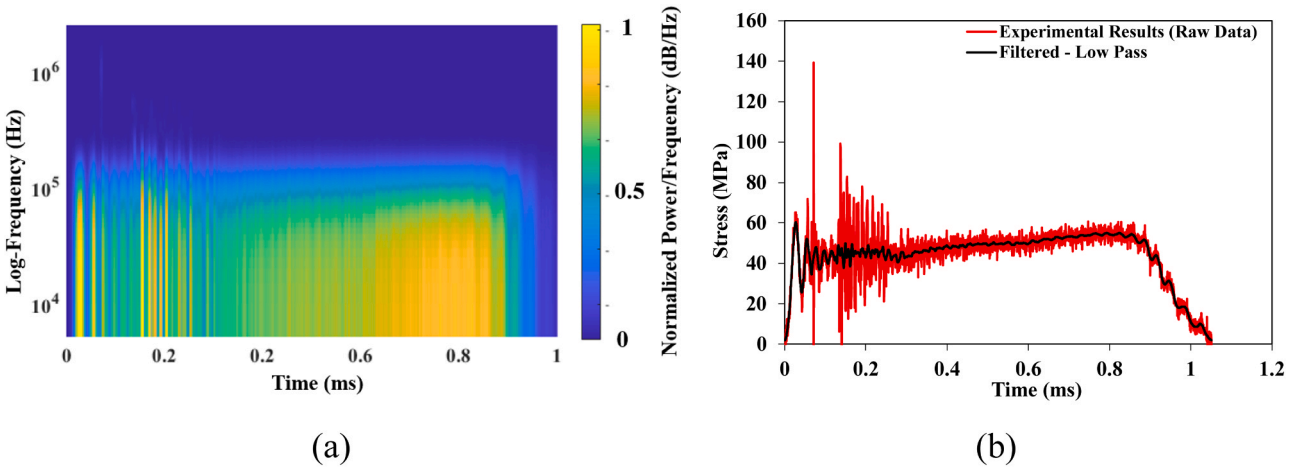

Fig. 5. (a) STFT spectrum analysis of a strain-voltage measured in the Hopkinson bar setup and (b) representative stress-time results tests with the cut-off filtering of 50 kHz compared to a representative stress-time curve without filtering.

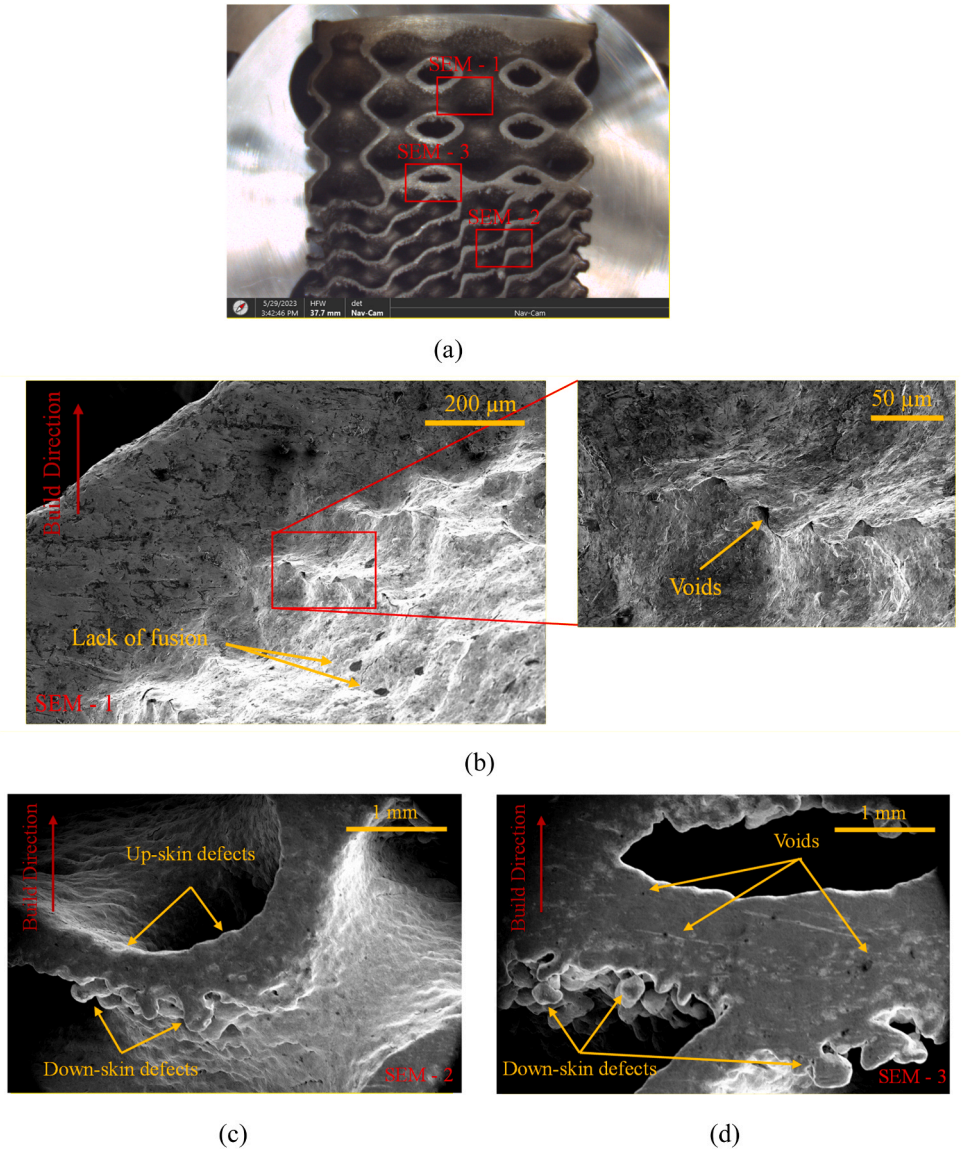

Fig. 6. (a) Optical microscope images from a sample with the metallurgical pores in red colour and (b), (c) and (d) SEM micrographs of a lattice structure unit cell showing the microdefects and voids on the specimen surface.

irregular voids containing un-melted powders [29,67].

Down-skin and up-skin surface defects were noticed on the resulting lattice structures, as represented in Fig. 6c. Local overheating is often seen on down-skin surfaces due to numerous overhanging features in lattice structures [67]. However, the stair-case effect, commonly associated with AM processes, was not evidenced in the analysed images, as seen in Fig. 6b. As discussed by Al-Ketan [11], strut-base lattices are more prone to observe the stair-stepping effect than the surface-base lattices, with the stair-stepping effect reduction being attributed to the continuous inclination angle change in surface-based designs as TPMS [67].

3.2. Hybrid topology definition

The testing rig exhibits a blast loading consistency response over three repetitions, i.e., an initial steep peak force followed by an abrupt decay being minimised along the time, as shown in Fig. 7a. A crushing wave propagates from the impact end to the support end by assuming that the single shock wave model holds with non-overlapping of the reflected elastic waves in the transmitted bar. Fig. 7b presents the cumulative impulse-time response for the three blast loading repetitions, which exhibit the good repeatability of the blast charging loading recorded in the transmitted bar. The experimental results show that at the initial crushing stage, the applied loading presents a peak average of 635.05 ± 9.81 kN, and the blast loading impulse imparted to the transmitted bar is 32.62 ± 0.92 N.s. The rig evaluation demonstrates the setup's applicability and performance. Furthermore, the force-time histories were compound and utilised as the transient pressure load in the finite element modelling.

To generate the desirability design criteria, 42 FE simulations were performed to fit the RSM response, as summarised in Appendix 1. Table 4 shows the analysis of variance (ANOVA), a statistical technique used to analyse the variation in data and determine the significance of the design variables in a designed experiment [63,72], where the *p-value* indicates the significance of the source (e.g., design variable) and their respective effect on the response surface variable. A *p-value* below a predetermined significance (usually denoted as α, commonly set to 0.05) indicates a greater significance of the variable on the measured response, i.e., indicating that the source studied presents a statistically significant impact on the response variable. A *p-value* above the significative value suggests a statistically insignificant effect on the response variable [51]. In the present study, the relative density of layer 1 and layer 2 (A-ρ^1_{rel} and B-ρ^2_{rel}, respectively) and the architecture type of layer 2 (D-L_2) have the most effect on the response.

Once the response surface is generated, the design variables can be optimised by setting the objective functions and the necessary constraints. The primary objective of this study is to maximise the SEA within the defined bounds for the relative densities. Fig. 8 shows the desirability chart for the various design variables and their responses, presenting the optimised solutions up to the 10th higher D-Efficiency. The desirability level evaluates and optimises multiple responses or variables simultaneously, evaluating the desirability or preference of the combinations of design variables on the maximisation of SEA value, expressed as a value between 0 and 1, where 0 indicates that the response or variable does not meet the desired requirement, and 1 represents the ideal or optimal design response that maximises the SEA value. The configuration of Gyroid being utilised in the two layers with $\rho^1_{rel} = 21.5\%$ and $\rho^2_{rel} = 20.5\%$ presents the maximum SEA from the DoE analysis. The top three and bottom three desirability configurations are chosen for the experimental evaluation analysis. From Fig. 8a, it is noticeable that the desirability levels increase within the lower relative density variable, in conclusion, for the tailor initial blast pressure, the lattices with lower relative density will present higher SEA capabilities. Also, Fig. 8b presents the efficiency of topologies for the constraints proposed in the DoE analysis, showing a consistency efficiency along the lattice architectures except for the Neovius lattice structure, which presents low desirability patterns. Table 5 summarises the chosen configurations of hybrid TPMS lattices to be experimentally tested, ρ^i_{rel}, the relative density, i the lattice position as shown in Fig. 2(a).

Table 4
Summary of the analysis of variance (ANOVA) results for the RSM response using DoE.

Source	*p-value*
Model	< 0.0001
A-ρ^1_{rel}	< 0.0001
B-ρ^2_{rel}	< 0.0001
C-L_1	0.0064
D-L_2	< 0.0001
A-ρ^1_{rel} and B-ρ^2_{rel}	0.0045
A-ρ^1_{rel} and C-L_1	0.5113
A-ρ^1_{rel} and D-L_2	0.7449
B-ρ^2_{rel} and C-L_1	0.8625
B-ρ^2_{rel} and D-L_2	0.0824
C-L_1 and D-L_2	0.5568

3.3. Experimental blast test results

Fig. 9(a -f) present the lattice structures before and after the blast impact, showing the crushing uniformity in the specimen and overall

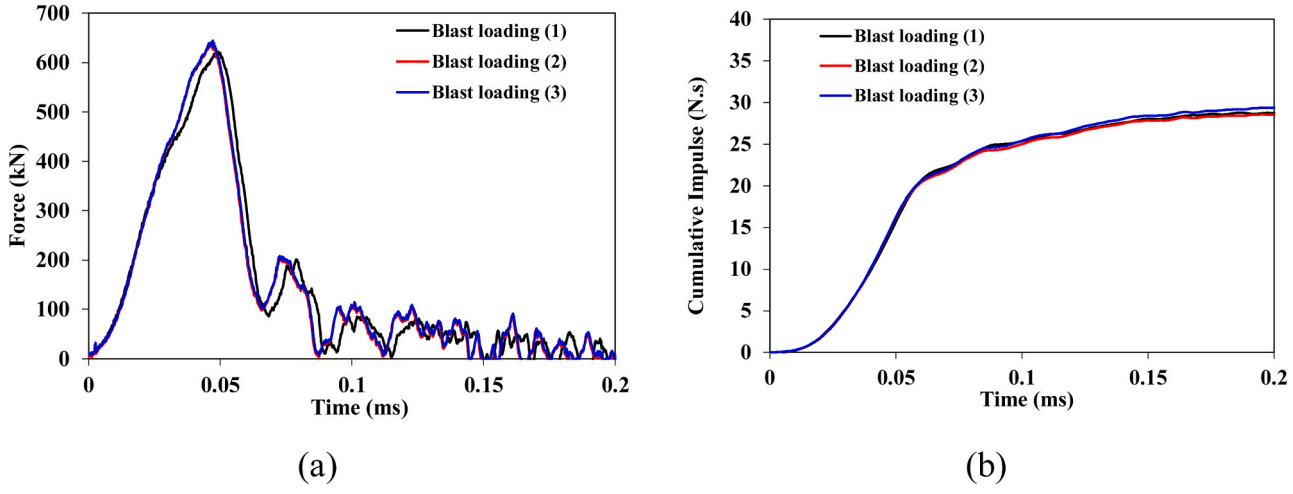

Fig. 7. Blast loading (a) force-time response and (b) cumulative impulse measured by the BHPB using 30 g PE10 explosive charge.

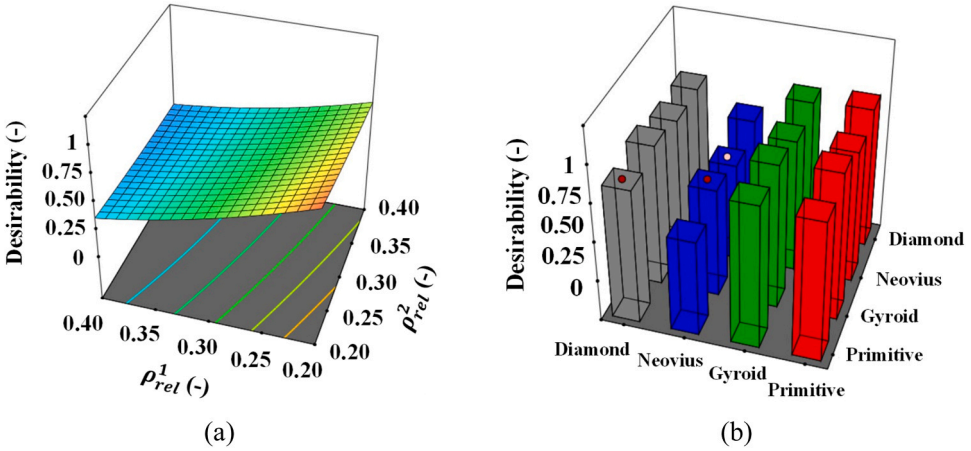

Fig. 8. Desirability response for (a) relative density and (b) topology architecture.

Table 5
Lattice nomenclature and respective lattice topology and relative density.

Sample	Layer 1	ρ^1_{rel} (%)	Layer 2	ρ^2_{rel} (%)	Desirability (-)
g22g20	Gyroid	21.5	Gyroid	20.4	1
d22p20	Diamond	21.7	Primitive	20.1	0.993645
d20g21	Diamond	20.0	Gyroid	21.0	0.977616
d40p40	Diamond	39.8	Primitive	39.9	0.410581
p38d40	Primitive	37.7	Diamond	39.9	0.410194
d38d40	Diamond	37.9	Diamond	39.9	0.357561

deformation aspects. The layered-hybrid lattice deformation behaviour and failure modes exhibit similarities across the samples, with unit cells collapsing through non-visible catastrophic brittle fracture due to the ductile ability of AM SS316L samples with high densification levels [10,18,27]. Under blast loading, the lattice displays a typical bending-dominated response with substantial ductile deformations, with the non-local collapse of a unit cell, as noted in [73]. However, the hybrid lattice exhibits high deformations, and the layering topology and relative density affect the compressive response qualitatively.

With a close examination of the high-speed images, higher deformations are observable for lattices with lower relative density. Additionally, different lattice combinations exhibit localised compressive plastic deformations triggered by layers. The triggering of compressive layering is noticeable in the d22p20 (Fig. 10b) and d20g21 (Fig. 10c) topologies, where the lattices being first compressed are primitive and diamond, respectively, until full layer densification, followed by the compressive triggering of the subsequent topological layer. Also, from the high-speed images, it is possible to highlight that the crushing of the structure is triggered at different layer positions, e.g., d22p20 (Fig. 10b) and p38d40 (Fig. 10f), which is affected by the direction of compression dictated by the anvil, indicating a homogeneous distribution of the compressive loading throughout the specimen.

Lattice topologies with a higher relative density, e.g., d40p40 (Fig. 10e) and p38d40 (Fig. 10f), exhibit lower deformations, as the compression is triggered solely by a unique lattice, where the blast loading impulse was inadequate to trigger the subsequent layer crushing. This suggests that the layer compressive triggering of the hybrid lattice structures is strictly related to the yield stress level of the topology. This evidence can also be correlated to similar dynamic compressive behaviour analyses conducted in the authors' previous work [10], where the plateau stress level varies for different architectures and relative densities.

Cross-sectional analyses are also vital to characterise the ductile failure mode, as shown in Fig. 11. Visible ductile compression of the lattice unit cell layers can be observed from the deformed cross-sectional images with the bending-dominated deformation mechanism [73]. In the first stage, the layers collapse singly for the layered-hybrid lattice with different architectures, forming two densified lattice regions, e.g., d22p20 (Fig. 11b) and d20g21 (Fig. 11c). This effect is not visible for lattices with similar topologies, i.e., g22g20 (Fig. 11a) and d38d40 (Fig. 11d), despite presenting changes in relative density layering. In the second process, shearing fracture can also be noticed in architecture primitive with higher relative density, e.g., d40p40 (Fig. 11e) and p38d40 (Fig. 11f). This fracture phenomenon is present due to the excessive deformation during compression led by material failure, as ductile bending deformations result in the shearing of the cell's connectivity.

The force histories recorded in the BHPB are shown in Fig. 12. It can be observed that the force-time curves of the layered-hybrid samples exhibit a reduction of load levels when compared to the un-sampled blast loading (Fig. 8a). Besides, as a high-strength material, the specimens present a high impedance and localised strain bands during compression, leading to load distribution along the blast compressive deformation. This layered-lattice compressive force-time behaviour presents a similarity to cellular foam structures, where there is a steep rise in the elastic region followed by a load plateau until densification [74]. Although only localised layering densification can be observed in some specimens, as shown in Fig. 11 (i.e., d22p20, d20g21, d40p40, and p38p40).

The force-time curves of the layered-hybrid lattice exhibit two distinct characteristics: Case (I) lattices have a homogenous and stable force distribution along the plateau region, while Case (II) lattices have more than one force plateau region along the compressive deformation. In both cases, the elastic region is relatively linear and similar, with force oscillations occurring before reaching the stable load plateau. These oscillations suggest that the topology unit cells experience localised yielding. For Case (I) lattices, the plateau region extends with a globalised densification of the topology until the load drops. This behaviour is evident in specimens with similar layered architectures, i.e., g22g20 (Fig. 12a) and d38d40 (Fig. 12d), as shown in the qualitative images (Fig. 10). For Case (II) lattices, as the compression continues, the first lattice layering almost reaches compactness, leading to a localised densification and a load transition related to the second linear elastic region, followed by a secondary plateau region. This phenomenon is visible in lattices with lower relative density, i.e., d22p20 (Fig. 12b) and d20g21 (Fig. 12c), as the blast loading generates large deformation resulting in high strain levels. Higher relative density lattices and different layering architectures, i.e., d40p40 (Fig. 12e) and p38d40 (Fig. 12f), characterise Case (II). These lattices have an elevated load plateau region compared to those with lower relative density. However, the transition region is not evident due to the insufficient blast energy supplied, an effect predicted by the DoE analysis.

The stress-strain history measurements using the BHPB and high-

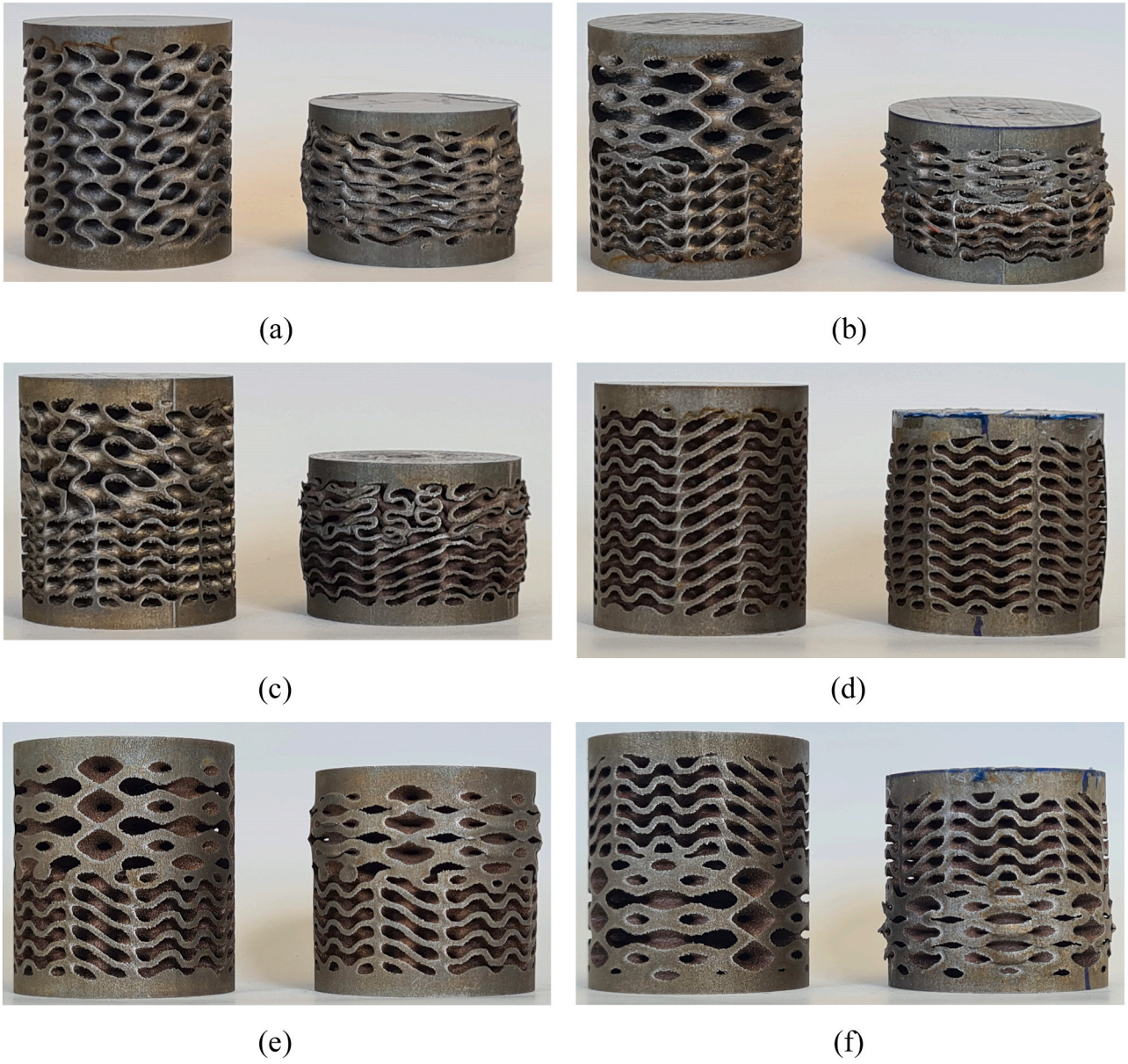

Fig. 9. Compressed and non-compressed lattices (a) g22g20, (b) d22p20, (c) d20g21, (d) d38d40, (e) d40p40, (f) p38d40.

speed camera are shown in Fig. 13. Initially, a relatively steep rise in the stress response curve is observed, characterised by an elastic region followed by a stress plateau region. The relatively high degree of linearity in the elastic region suggests a global yielding of the layered-hybrid lattices. This indicates a stable hierarchical structure with repeated unit cells along the layers, as observed by different authors [29,75]. The elastic region of the stress-strain curves presents similar slopes for all specimen configurations attenuated by attaining their respective lattice layering yield stress followed by a plateau strength. A smooth transition between the elastic and plateau regions can be observed for all structures subjected to blast loading. However, visible fluctuations are attenuated in the transition between elastic and plateau stress regions but reduced along the compressive deformation. The first peak stress presented in the fluctuation occurs at around 31 μs and is presumed to be caused by elastic wave propagation in the anvil. With the blast loading generated by the charge, elastic waves are generated in the anvil. Although the anvil inertial effect compresses the hybrid lattices, elastic waves generated during the blast load produce an evident stress oscillation at a constant frequency.

Localised layer densification can be observed for the lattices independent of their relative densities. From Fig. 13(b)-(c), the qualitative images show that the stress transition in layered-hybrid lattices with a lower relative density, i.e., d22p20 (Fig. 13b) and d20g21 (Fig. 13c), happens due to localised layer densification and transition yield to plateau stress of the subsequent hybrid layer. A similar effect can also be observed from lattices with a higher relative density, i.e., d40p40 (Fig. 13e) and p38d40 (Fig. 13f). However, their plateau region is triggered and dominated by one of the layering architectures, which requires a higher blast load to compress the hybrid layer below. Additionally, the layer triggering is strictly linked to the topology yield level, as demonstrated by the architectures with different layering architectures, i.e., d22p20 (Fig. 13b), d20g21 (Fig. 13c), d40p40 (Fig. 13e), and p38p40 (Fig. 13f), which is not attributed to the direction of compression. Qualitative images also provide an overview of where the lattice governs plateau region values with lower yield stress. After full layering densification, the stress values increase until the yield stress of the lattices below. Although the lattice structures with higher relative density studied here do not reach the onset of full densification, the

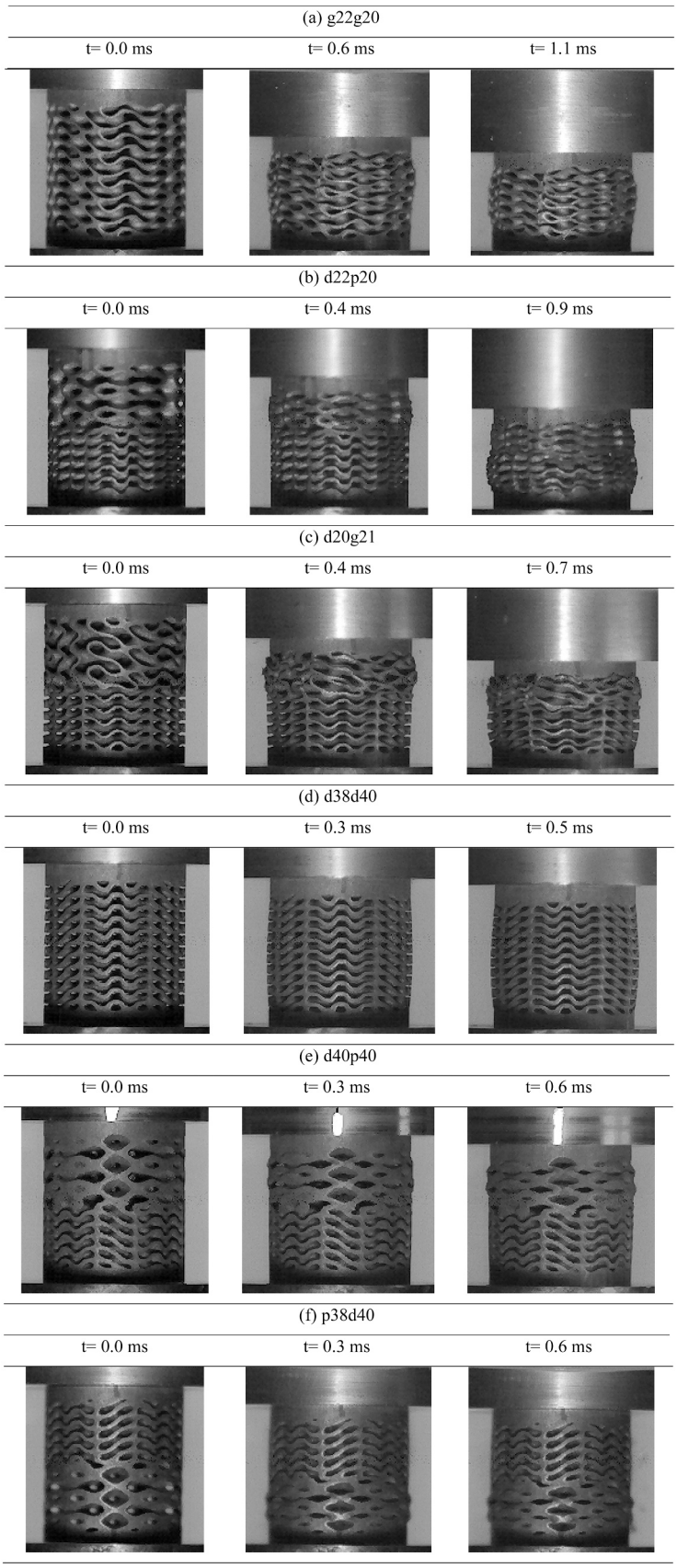

Fig. 10. Comparison of the evolution of the deformation mode comparison for the different lattice topologies.

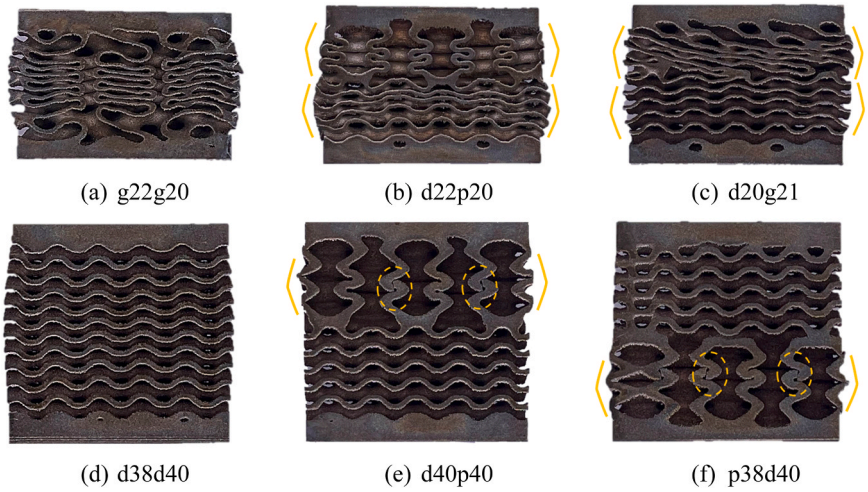

Fig. 11. Cross-section comparison of the different lattice topologies.

hybrid lattice g22g20 (Fig. 13a) presents the highest stress-strain relationship and deformation level, correlating to the prediction of DoE analysis.

Fig. 14 shows the strain-rate evolution on the hybrid lattice structures subjected to blast load. The results show a difference between the strain-rate evolution for the hybrid lattice configurations, where lattices with higher relative density show lower maximum strain-rate values than those with lower relative density. Due to the higher plateau region and stiffness, the deformation velocity experienced in those cases is higher when compared to the higher relative density lattices. Although the blast tests presented elevated strain-rate levels, other authors reached similar levels using the direct impact Hopkinson bar technique [10,55,75]. This can be related to the hybrid lattice's stiffness and relative density [18], with overall dimension characteristics directly affecting strain-rate levels.

Fig. 15 compares crashworthiness parameters for the hybrid lattices studied, where the experimental results are summarised in Table 6. The compressive mechanical behaviour of each hybrid topology is compared in terms of the impulse, maximum strain, peak force, and SEA. Fig. 15a shows that all the structures exhibit stable impulse values, presenting an average of 32.36 ± 1.47 N.s among all the topologies studied. These results give evidence that the instrumented BHPB setup is successfully employed for impact due to the consistency of load-time applied. However, the strain rate employed during impact shows slightly lower values when compared with the results obtained from the direct impact technique [10,55,75]. The presented variant subjects the specimen to the conditions of dynamic forces for similar conditions in a blast environment. Besides, the instrumented Hopkinson bar allows for an easy specimen installation and provides a straightforward approach for evaluating the results with a simplified process for blast characterisations.

Fig. 15b shows the maximum strain values for the layered-hybrid lattices studied. The deformation values were compounded by the maximum strain presented in the stress-strain response. An evident difference between the lattices can also be highlighted, where lattices with lower relative density (i.e., g22g20, d22p20, and d20g21) present an increase of 265% in the maximum strain when compared to higher relative densities topologies (i.e., d40p40, p38d40, and d38d40). Also, the peak force analysis presented in Fig. 15c shows that the specimens are also significantly divergent in their maximum force levels. The peak load has shown a similar feature as the maximum strain (Fig. 15b). In the case of topologies with a lower relative density, peak force reduction can be identified on the transmitted bar. This is clear evidence of differences in stiffness due to the relative density of the lattices studied, which have already been investigated by several authors [10,15,52,76,77]. Moreover, the charging load amplitude is absorbed as the lattice unit cells go through a relatively stable load plateau region, with an average of 88% peak force reduction compared with the blast loading evaluation (Fig. 8a).

Based on the SEA parameter, the energy is limited to the deformation observed corresponding to ε_{max} obtained. The SEA values for each lattice topology are presented in Fig. 15d. For a higher relative density (~40%), the SEA is 52.3% smaller than a lower relative density (~20%) because of its less efficient cell architecture than the lower relative density one. Also, the densification strain of the former is smaller than the latter, decreasing the energy absorption capacity. The differences in densification strain are partly attributed to the blast loading not being sufficient to fully densify the hybrid lattices with higher relative density. However, the criterion for defining the densification strain, based on the maximum energy absorption efficiency point, influences the results, which seems to validate the layered-lattice prediction based on the Desirability results. The DoE results provide a good prediction of the overall behaviour of the layered-hybrid lattice structures, capturing the different energy absorption responses.

The length of the transmitted bar (~4.5 m), the location of the strain gauges, and the duration of the impact event ensure that the reflected wave signals do not affect the test. However, certain implications may arise due to the frequency content of the wave and the bar diameter, which could induce wave dispersion [78,79]. The use of pulse smothering can reduce high-frequency content, as demonstrated in Ref. [59]. In this BHPB evaluation, the gauge position of 750 mm from the specimen face reduces wave dispersion to a non-significant level. However, the superposition of signal waves can still occur due to pulse duration caused by a higher quantity of charging mass. This method holds immense potential for further improvement and development, particularly for high-rate levels of stiffer specimens exposed to the peak pressure of blast load with changing conditions. Moreover, high-speed imaging techniques were utilised to measure the displacements and strain rates of the specimen, which enabled the determination of SEA values to assess a structure's energy-absorbing capacity under hazardous blast loading conditions.

Analysing the performance of blast-resistant structures subjected to near-field to high explosive detonations is critical to obtain information of energy absorption levels. In structures placed near a high explosive detonation source, the resulting pressure is of immense magnitude and exhibits highly non-uniform distribution across the target surface [57–59]. While the load is uniformly distributed in the designed BPHB setup, the quantity of charging mass remains limited. As discussed previously, the direct measurement of blast parameters is restricted due to the lack of instrumentation that can withstand extreme loading

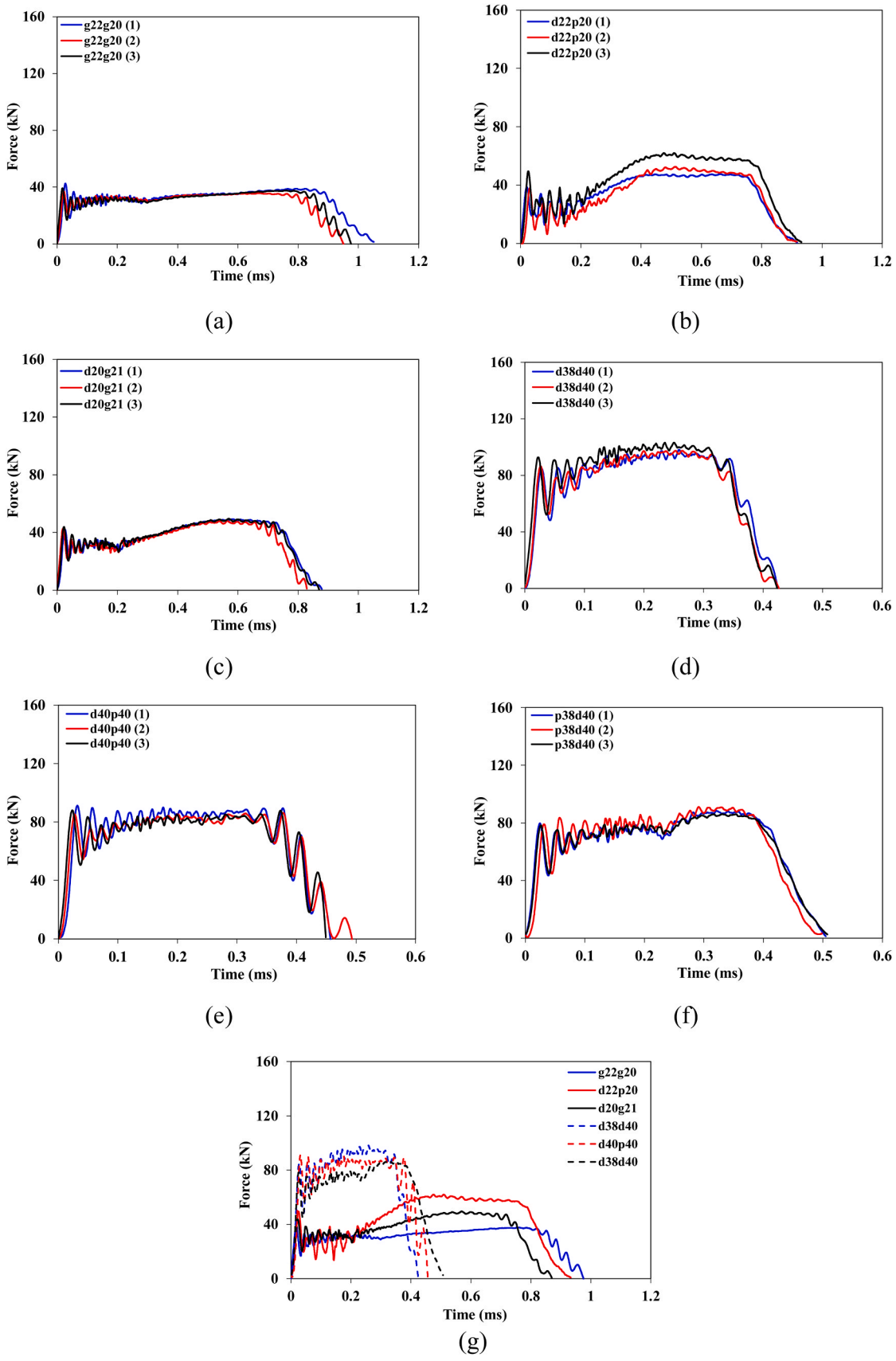

Fig. 12. Force-time histories of the different layering-hybrid lattices (a) g22g20, (b) d22p20, (c) d20g21, (d) d38d40, (e) d40p40, (f) p38d40, and (g) comparison of different lattices.

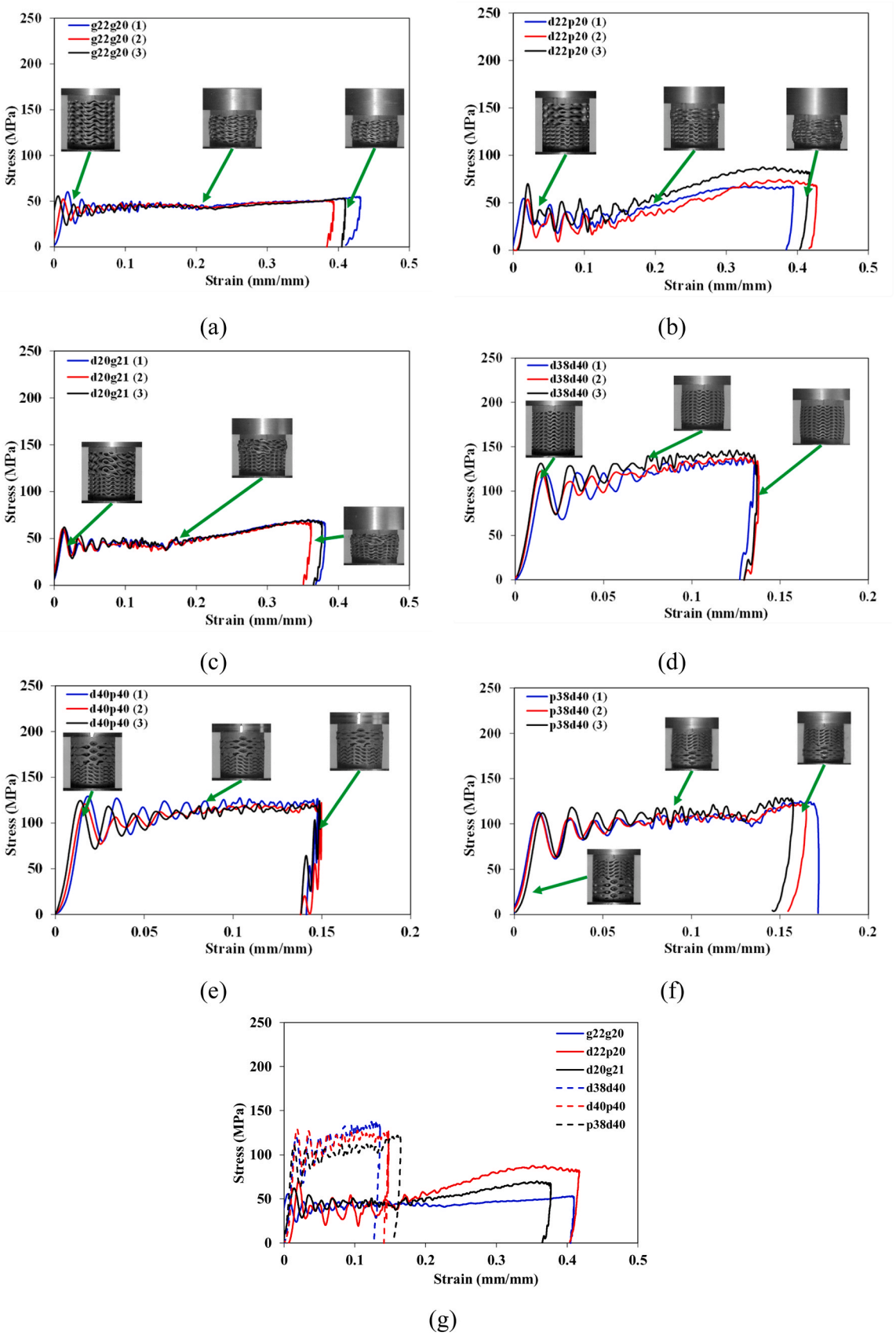

Fig. 13. Stress-strain relationships of different lattice architectures (a) g22g20, (b) d22p20, (c) d20g21, (d) d38d40, (e) d40p40, (f) p38d40, and (g) comparison of different lattices.

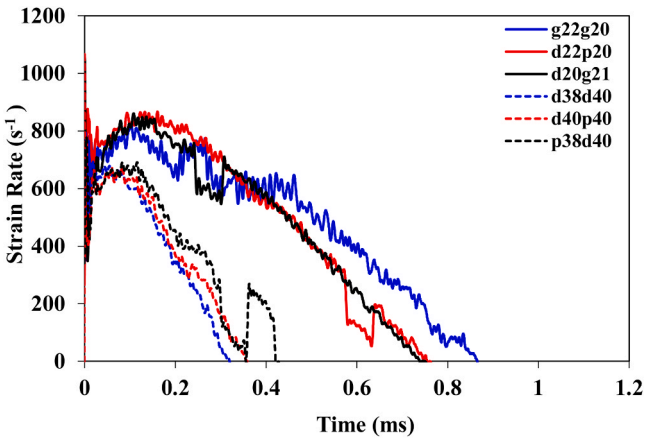

Fig. 14. Strain-rate evolution of hybrid lattice structures subjected to blast loadings.

conditions. The proposed BHPB method is to overcome these challenges, enabling a clear understanding of the crushing behaviour of hybrid-layered lattice structures. However, the combined analysis of kinematic pressure with fragmentation is still limited. This approach minimises the influence of fireball and detonation [60], allowing clear observations from spatial and temporal pressure measurements from near-field explosions.

In conclusion, the proposed methodology effectively utilises a design-based (i.e., DoE) approach to select lattice architectures and experimentally evaluate them under blast loading conditions instead of conducting systematic tests on various non-tailored topology configurations. These design parameters can be modified by tailoring the topologies and relative density to achieve tailored shock-wave requirements, thus modifying the SEA capabilities, peak force, and maximum strain. For instance, lattices with a higher blast energy absorption could be ideal for armouring protection/cladding with high compressibility shapes, e.g., vehicle armouring. This indicates that DoE lattices could be particularly advantageous in applications that require an engineered crushing response, e.g., aerospace, automotive, and personal protection applications. Although the blast compressive behaviour of optimised cladding hybrid structures has been studied, further research is needed to investigate their response to combined ballistic and blast protection.

4. Conclusions

This study has investigated the blast compressive behaviour of different hybrid layered lattice structures made with stainless steel (SS316L) using AM technique. The research findings provide valuable insights into the performance of these structures under blast loading conditions, addressing the research questions regarding their suitability

Table 6
Summary of the experimental crashworthiness of hybrid-layered lattice structures under blast loading conditions.

Lattices Type	Impulse (N.s)	ε_{max} (mm/mm)	Peak Force (kN)	SEA (J/g)
g22g20	30.44 ± 1.97	0.4115 ± 0.0189	39.61 ± 2.80	8.11 ± 0.45
d22p20	34.47 ± 4.82	0.4130 ± 0.0169	53.97 ± 7.29	7.93 ± 0.42
d20g21	31.14 ± 1.19	0.3734 ± 0.0104	48.93 ± 0.77	8.01 ± 0.56
d38d40	32.26 ± 1.16	0.1369 ± 0.0011	99.55 ± 3.12	4.12 ± 0.25
d40p40	32.40 ± 0.41	0.1489 ± 0.0010	88.48 ± 2.54	4.10 ± 0.19
p38d40	33.47 ± 0.18	0.1648 ± 0.0072	100.42 ± 18.61	4.36 ± 0.33

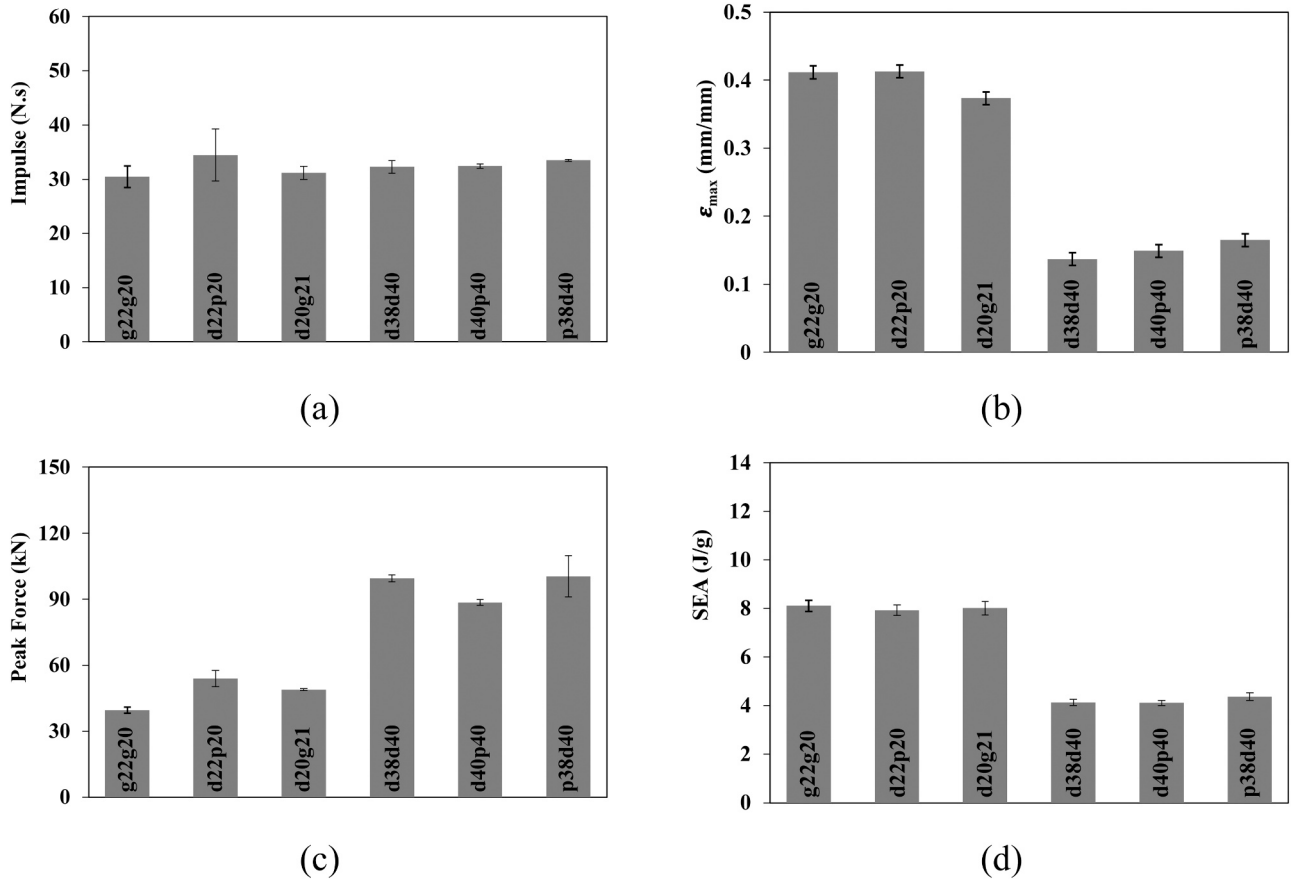

Fig. 15. Comparison of hybrid-layered lattice structure crashworthiness (a) peak specific impulse, (b) maximum strain, (c) peak force, and (d) SEA.

for tailored design requirements. The following conclusions can be drawn based on the current research outcomes.

- A proposed blast rig has been designed and evaluated based on the Hopkinson bar technique. Results show that the BHPB rig can reliably measure the energy absorption of protective structures subjected to near-field to high explosive detonations, although the combined analysis of kinematic pressure with fragmentation is still limited.
- DoE methodology is effective for systematically evaluating different hybrid lattice configurations and identifying the optimal design for shock-wave absorption.
- An experimental blast campaign on layered-hybrid lattice structures has been successfully conducted in compressive blast loading. The proposed lattices investigated have shown high energy absorption capabilities against blast loading, with no significant damage and maintaining structural integrity.
- Hybrid-layered lattices have demonstrated different cases of compression, showing a significant influence on their stress-strain response by the layered triggering. The triggering of crushing initiation is closely related to the lattice's yield stress level.

This experimental study, evaluation and analysis highlight the significant potential of hybrid lattice structures in the tailored design using DoE. These structures have shown promise in various applications, including defence, protective barriers, armour systems, and critical locations of infrastructures such as buildings, bridges, and tunnels, where enhancing resistance to blast events is crucial. Additionally, such structures have potential relevance in industries exposed to explosive or high-pressure environments like oil and gas, mining, and chemical processing. These structures exhibit high energy absorption capabilities, making them an attractive option for high-velocity shock wave impact scenarios. A more detailed study and simulations verification of the TPMS topologies and their influence on blast performance is suggested for further study. The findings of this study contribute to advancing knowledge in blast-resistant design and provide valuable insights for future research and development in this field.

CRediT authorship contribution statement

Rafael Santiago: Writing – review & editing, Supervision, Investigation. **Jide Oyebanji:** Investigation. **Kapil Krishnan:** Writing – review & editing, Investigation. **Genevieve Langdon:** Writing – review & editing, Investigation. **Zhongwei Guan:** Writing – review & editing, Supervision. **Henrique Ramos:** Writing – review & editing, Writing – original draft, Investigation. **Sara AlMahri:** Investigation. **Erik Pickering:** Writing – review & editing, Investigation.

Declaration of Competing Interest

The authors declare that they have no known competing financial interests or personal relationships that could have appeared to influence the work reported in this paper.

Data Availability

Data will be made available on request.

Acknowledgements

This work was supported by the Advanced Technology Research Council (ATRC) in Abu Dhabi, UAE.

Appendix 1

Table A1
DoE response with design variable and desirability response.

Run	Layer 1	ρ^{I}_{rel} (-)	Layer 2	ρ^{I}_{rel} (-)	Desirability (-)
1	Gyroid	0.30	Gyroid	0.20	0.886534
2	Gyroid	0.20	Gyroid	0.30	0.700702
3	Primitive	0.35	Primitive	0.35	0.487763
4	Diamond	0.30	Primitive	0.35	0.513423
5	Primitive	0.20	Diamond	0.20	0.966847
6	Primitive	0.20	Primitive	0.40	0.444676
7	Diamond	0.40	Gyroid	0.30	0.570018
8	Diamond	0.30	Diamond	0.20	0.830309
9	Diamond	0.40	Diamond	0.40	0.352756
10	Gyroid	0.20	Neovius	0.40	0.34593
11	Gyroid	0.25	Primitive	0.30	0.668414
12	Neovius	0.40	Gyroid	0.20	0.733786
13	Primitive	0.30	Neovius	0.25	0.458713
14	Gyroid	0.40	Neovius	0.40	0.265134
15	Diamond	0.30	Gyroid	0.40	0.404479
16	Gyroid	0.20	Neovius	0.20	0.78897
17	Primitive	0.40	Diamond	0.30	0.515918
18	Neovius	0.35	Neovius	0.30	0.308353
19	Neovius	0.40	Diamond	0.40	0.316886
20	Diamond	0.25	Diamond	0.35	0.48818
21	Diamond	0.30	Gyroid	0.20	0.897474
22	Primitive	0.30	Diamond	0.40	0.385444
23	Neovius	0.30	Neovius	0.20	0.700784
24	Gyroid	0.20	Diamond	0.40	0.431297
25	Neovius	0.40	Primitive	0.20	0.720062
26	Primitive	0.25	Gyroid	0.30	0.667976
27	Primitive	0.40	Primitive	0.20	0.770166
28	Gyroid	0.40	Gyroid	0.40	0.365906
29	Diamond	0.20	Primitive	0.40	0.446973
30	Gyroid	0.35	Neovius	0.30	0.351646
31	Primitive	0.35	Gyroid	0.25	0.727985
32	Diamond	0.20	Neovius	0.40	0.344035

(*continued on next page*)

Table A1 (*continued*)

Run	Layer 1	ρ^{l}_{rel} (-)	Layer 2	ρ^{l}_{rel} (-)	Desirability (-)
33	Neovius	0.40	Neovius	0.20	0.555679
34	Neovius	0.20	Diamond	0.30	0.614588
35	Diamond	0.35	Primitive	0.25	0.705074
36	Gyroid	0.30	Gyroid	0.35	0.52223
37	Gyroid	0.40	Diamond	0.20	0.770607
38	Primitive	0.25	Primitive	0.25	0.800126
39	Primitive	0.40	Neovius	0.40	0.262086
40	Neovius	0.20	Primitive	0.40	0.401337
41	Neovius	0.20	Gyroid	0.40	0.401459
42	Neovius	0.30	Primitive	0.25	0.650446

References

[1] M. Stanczak, T. Fras, L. Blanc, P. Pawlowski, A. Rusinek, Numerical and experimental study on mechanical behaviour of the AlSi10Mg aluminium structures manufactured additively and subjected to a blast wave, EPJ Web Conf. 250 (2021) 02017, https://doi.org/10.1051/epjconf/202125002017.

[2] M. Stanczak, T. Fras, L. Blanc, P. Pawlowski, A. Rusinek, Blast-induced compression of a thin-walled aluminum honeycomb structure—experiment and modeling, Metals 9 (2019), https://doi.org/10.3390/met9121350.

[3] G. Sun, E. Wang, J. Zhang, S. Li, Y. Zhang, Q. Li, Experimental study on the dynamic responses of foam sandwich panels with different facesheets and core gradients subjected to blast impulse, Int. J. Impact Eng. 135 (2020), 103327, https://doi.org/10.1016/j.ijimpeng.2019.103327.

[4] X. Jin, Z. Wang, J. Ning, G. Xiao, E. Liu, X. Shu, Dynamic response of sandwich structures with graded auxetic honeycomb cores under blast loading, Compos. Part B Eng. 106 (2016) 206–217, https://doi.org/10.1016/j.compositesb.2016.09.037.

[5] Y. Ding, S. Wang, K. Zhao, Z. Zheng, L. Yang, J. Yu, Blast alleviation of cellular sacrificial cladding: a nonlinear plastic shock model, Int. J. Appl. Mech. 08 (2016) 1650057, https://doi.org/10.1142/S1758825116500575.

[6] H. Andami, H. Toopchi-Nezhad, Performance assessment of rigid polyurethane foam core sandwich panels under blast loading, Int. J. Prot. Struct. 11 (2020) 109–130, https://doi.org/10.1177/2041419619858091.

[7] D. Karagiozova, G.S. Langdon, G.N. Nurick, Propagation of compaction waves in metal foams exhibiting strain hardening, Int. J. Solids Struct. 49 (2012) 2763–2777.

[8] G.S. Langdon, D. Karagiozova, M.D. Theobald, G.N. Nurick, G. Lu, R.P. Merrett, Fracture of aluminium foam core sacrificial cladding subjected to air-blast loading, Int. J. Impact Eng. 37 (2010) 638–651.

[9] D. Karagiozova, G.S. Langdon, G.N. Nurick, Blast attenuation in Cymat foam core sacrificial claddings, Int. J. Mech. Sci. 52 (2010) 758–776.

[10] S. AlMahri, R. Santiago, D. Lee, H. Ramos, H. Alabdouli, M. Alteneiji, Z. Guan, W. Cantwell, M. Alves, Evaluation of the dynamic response of triply periodic minimal surfaces subjected to high strain-rate compression, Addit. Manuf. (2021), 102220, https://doi.org/10.1016/j.addma.2021.102220.

[11] O. Al-Ketan, R. Rowshan, R.K.Abu Al-Rub, Topology-mechanical property relationship of 3D printed strut, skeletal, and sheet based periodic metallic cellular materials, Addit. Manuf. 19 (2018) 167–183, https://doi.org/10.1016/j.addma.2017.12.006.

[12] A.M. Abou-Ali, O. Al-Ketan, D.W. Lee, R. Rowshan, R.K.Abu Al-Rub, Mechanical behavior of polymeric selective laser sintered ligament and sheet based lattices of triply periodic minimal surface architectures, Mater. Des. 196 (2020), 109100, https://doi.org/10.1016/j.matdes.2020.109100.

[13] T. Tancogne-Dejean, D. Mohr, Stiffness and specific energy absorption of additively-manufactured metallic BCC metamaterials composed of tapered beams, Int. J. Mech. Sci. 141 (2018) 101–116, https://doi.org/10.1016/j.ijmecsci.2018.03.027.

[14] J.Y. Liu, H.T. Liu, M.R. An, Crushing behaviors of novel Diabolo shaped honeycombs with enhanced energy absorption performance, Int. J. Mech. Sci. 229 (2022), 107492, https://doi.org/10.1016/j.ijmecsci.2022.107492.

[15] N. Jin, F. Wang, Y. Wang, B. Zhang, H. Cheng, H. Zhang, Failure and energy absorption characteristics of four lattice structures under dynamic loading, Mater. Des. 169 (2019), 107655, https://doi.org/10.1016/j.matdes.2019.107655.

[16] J.M. Jafferson, H. Sharma, Design of 3D printable airless tyres using NTopology, Mater. Today Proc. 46 (2021) 1147–1160, https://doi.org/10.1016/j.matpr.2021.02.058.

[17] A.A. Naderi, Blast resistance of an innovative helmet liner composed of an auxetic lattice, Struct., AUT J. Mech. Eng. 6 (2022), 4–4.

[18] S. McKown, Y. Shen, W.K. Brookes, C.J. Sutcliffe, W.J. Cantwell, G.S. Langdon, G. N. Nurick, M.D. Theobald, The quasi-static and blast loading response of lattice structures, Int. J. Impact Eng. 35 (2008) 795–810.

[19] Z. Ozdemir, E. Hernandez-Nava, A. Tyas, J.A. Warren, S.D. Fay, R. Goodall, I. Todd, H. Askes, Energy absorption in lattice structures in dynamics: experiments, Int. J. Impact Eng. 89 (2016) 49–61, https://doi.org/10.1016/j.ijimpeng.2015.10.007.

[20] B.J. Ramirez, U. Misra, V. Gupta, Viscoelastic foam-filled lattice for high energy absorption, Mech. Mater. 127 (2018) 39–47, https://doi.org/10.1016/j.mechmat.2018.08.011.

[21] G. Feng, J. Wang, X. Li, L. Xiao, W. Song, Mechanical behavior of Ti–6Al–4V lattice-walled tubes under uniaxial compression, Def. Technol. 18 (2022) 1124–1138, https://doi.org/10.1016/j.dt.2021.05.012.

[22] D. Karagiozova, G.S. Langdon, Impact of cellular materials, in: Encycl. Contin. Mech, Springer Berlin Heidelberg, Berlin Heidelberg, 2020, pp. 1266–1287, https://doi.org/10.1007/978-3-662-55771-6_203.

[23] L. Xiao, W. Song, X. Xu, Experimental study on the collapse behavior of graded Ti-6Al-4V micro-lattice structures printed by selective laser melting under high speed impact, Thin-Walled Struct. 155 (2020), 106970, https://doi.org/10.1016/j.tws.2020.106970.

[24] Z. Zheng, J. Yu, C. Wang, S. Liao, Y. Liu, Dynamic crushing of cellular materials: a unified framework of plastic shock wave models, Int. J. Impact Eng. 53 (2013) 29–43, https://doi.org/10.1016/j.ijimpeng.2012.06.012.

[25] G. Imbalzano, S. Linforth, T.D. Ngo, P.V.S. Lee, P. Tran, Blast resistance of auxetic and honeycomb sandwich panels: comparisons and parametric designs, Compos. Struct. 183 (2018) 242–261, https://doi.org/10.1016/j.compstruct.2017.03.018.

[26] Y. Zhang, T. Liu, H. Ren, I. Maskery, I. Ashcroft, Dynamic compressive response of additively manufactured AlSi10Mg alloy hierarchical honeycomb structures, Compos. Struct. 195 (2018) 45–59, https://doi.org/10.1016/j.compstruct.2018.04.021.

[27] M. Smith, W.J. Cantwell, Z. Guan, S. Tsopanos, M.D. Theobald, G.N. Nurick, G. S. Langdon, The quasi-static and blast response of steel lattice structures, J. Sandw. Struct. Mater. 13 (2011) 479–501, https://doi.org/10.1177/1099636210388983.

[28] H. Ramos, R. Santiago, S. Soe, P. Theobald, M. Alves, Response of gyroid lattice structures to impact loads, Int. J. Impact Eng. (2022), 104202, https://doi.org/10.1016/j.ijimpeng.2022.104202.

[29] H.A. AlQaydi, K. Krishnan, J. Oyebanji, D.W. Lee, S.A. Alneyadi, N. Ghisi, L. Kindleyside, N.T. Aboulkhair, Hybridisation of AlSi10Mg lattice structures for engineered mechanical performance, Addit. Manuf. 57 (2022), 102935, https://doi.org/10.1016/j.addma.2022.102935.

[30] N. Novak, O. Al-Ketan, M. Borovinšek, L. Krstulović-Opara, R. Rowshan, M. Vesenjak, Z. Ren, Development of novel hybrid TPMS cellular lattices and their mechanical characterisation, J. Mater. Res. Technol. 15 (2021) 1318–1329, https://doi.org/10.1016/j.jmrt.2021.08.092.

[31] S.J. Cimpoeru, P. Phillips, D.V. Ritzel, A systems view of vehicle landmine survivability, Int. J. Prot. Struct. 6 (2015) 137–153.

[32] A.E. Medvedev, T. Maconachie, M. Leary, M. Qian, M. Brandt, Perspectives on additive manufacturing for dynamic impact applications, Mater. Des. 221 (2022), 110963, https://doi.org/10.1016/j.matdes.2022.110963.

[33] J. Banhart, Manufacture, characterisation and application of cellular metals and metal foams, Prog. Mater. Sci. 46 (2001) 559–632.

[34] Y. Sun, Q.M. Li, Dynamic compressive behaviour of cellular materials: a review of phenomenon, mechanism and modelling, Int. J. Impact Eng. 112 (2018) 74–115.

[35] Y. Wang, F. Liu, X. Zhang, K. Zhang, X. Wang, D. Gan, B. Yang, Cell-size graded sandwich enhances additive manufacturing fidelity and energy absorption, Int. J. Mech. Sci. 211 (2021), 106798, https://doi.org/10.1016/j.ijmecsci.2021.106798.

[36] C.G. Ferro, S. Varetti, P. Maggiore, M. Lombardi, S. Biamino, D. Manfredi, F. Calignano, Design and characterization of trabecular structures for an anti-icing sandwich panel produced by additive manufacturing, J. Sandw. Struct. Mater. 22 (2020) 1111–1131.

[37] G. Imbalzano, P. Tran, T.D. Ngo, P.V.S. Lee, Three-dimensional modelling of auxetic sandwich panels for localised impact resistance, J. Sandw. Struct. Mater. 19 (2017) 291–316.

[38] C. Peng, P. Tran, Bioinspired functionally graded gyroid sandwich panel subjected to impulsive loadings, Compos. Part B Eng. 188 (2020), 107773, https://doi.org/10.1016/j.compositesb.2020.107773.

[39] P. Tran, C. Peng, Triply periodic minimal surfaces sandwich structures subjected to shock impact, J. Sandw. Struct. Mater. 23 (2021) 2146–2175, https://doi.org/10.1177/1099636220905551.

[40] N. Novak, M. Borovinšek, O. Al-Ketan, Z. Ren, M. Vesenjak, Impact and blast resistance of uniform and graded sandwich panels with TPMS cellular structures, Compos. Struct. 300 (2022), https://doi.org/10.1016/j.compstruct.2022.116174.

[41] R. Critchley, R. Hazael, K. Bhatti, D. Wood, A. Peare, S. Johnson, T. Temple, Blast mitigation using polymeric 3D printed auxetic re-entrant honeycomb structures: A preliminary study, Int. J. Prot. Struct. 13 (2022) 469–486, https://doi.org/10.1177/20414196211052062.

[42] Y. Wei, C. Zhang, Y. Yuan, P. Chen, C. Huang, J. Li, M. Yuan, Blast response of additive manufactured Ti–6Al–4V sandwich panels, Int. J. Impact Eng. 176 (2023), 104553, https://doi.org/10.1016/j.ijimpeng.2023.104553.
[43] N. Novak, L. Starčevič, M. Vesenjak, Z. Ren, Blast response study of the sandwich composite panels with 3D chiral auxetic core, Compos. Struct. 210 (2019) 167–178, https://doi.org/10.1016/j.compstruct.2018.11.050.
[44] A. Jankovic, G. Chaudhary, F. Goia, Designing the design of experiments (DOE)–an investigation on the influence of different factorial designs on the characterization of complex systems, Energy Build. 250 (2021), 111298.
[45] H.Y. Grisaro, A.N. Dancygier, Characteristics of combined blast and fragments loading, Int. J. Impact Eng. 116 (2018) 51–64, https://doi.org/10.1016/j.ijimpeng.2018.02.004.
[46] U. Nyström, K. Gylltoft, Numerical studies of the combined effects of blast and fragment loading, Int. J. Impact Eng. 36 (2009) 995–1005.
[47] J. Leppänen, Experiments and numerical analyses of blast and fragment impacts on concrete, Int. J. Impact Eng. 31 (2005) 843–860.
[48] V. Aune, E. Fagerholt, M. Langseth, T. Børvik, A shock tube facility to generate blast loading on structures, Int. J. Prot. Struct. 7 (2016) 340–366, https://doi.org/10.1177/2041419616666236.
[49] J. Liu, S. He, H. Zhao, G. Li, M. Wang, Experimental investigation on the dynamic behaviour of metal foam: From yield to densification, Int. J. Impact Eng. 114 (2018) 69–77, https://doi.org/10.1016/j.ijimpeng.2017.12.016.
[50] L. Li, B. Han, S.Y. He, Z.Y. Zhao, R. Zhang, Q.C. Zhang, T.J. Lu, Shock loading simulation using density-graded metallic foam projectiles, Mater. Des. 164 (2019), 107546, https://doi.org/10.1016/j.matdes.2018.107546.
[51] X. Li, L. Xiao, W. Song, Compressive behavior of selective laser melting printed Gyroid structures under dynamic loading, Addit. Manuf. 46 (2021), 102054, https://doi.org/10.1016/j.addma.2021.102054.
[52] T. Tancogne-Dejean, A.B. Spierings, D. Mohr, Additively-manufactured metallic micro-lattice materials for high specific energy absorption under static and dynamic loading, Acta Mater. 116 (2016) 14–28, https://doi.org/10.1016/j.actamat.2016.05.054.
[53] T. Tancogne-Dejean, X. Li, M. Diamantopoulou, C.C. Roth, D. Mohr, High strain rate response of additively-manufactured plate-lattices: experiments and modeling, J. Dyn. Behav. Mater. 5 (2019) 361–375, https://doi.org/10.1007/s40870-019-00219-6.
[54] D. Khrapov, A. Koptyug, K. Manabaev, F. Léonard, T. Mishurova, G. Bruno, D. Cheneler, K. Loza, M. Epple, R. Surmenev, M. Surmeneva, The impact of post manufacturing treatment of functionally graded Ti6Al4V scaffolds on their surface morphology and mechanical strength, J. Mater. Res. Technol. 9 (2020) 1866–1881, https://doi.org/10.1016/j.jmrt.2019.12.019.
[55] T. Fíla, P. Koudelka, J. Falta, P. Zlámal, V. Rada, M. Adorna, S. Bronder, O. Jirousek, Dynamic impact testing of cellular solids and lattice structures: application of two-sided direct impact Hopkinson bar, Int. J. Impact Eng. 148 (2021), https://doi.org/10.1016/j.ijimpeng.2020.103767.
[56] R.A. Govender, R.J. Curry, The “open” hopkinson pressure bar: towards addressing force equilibrium in specimens with non-uniform deformation, J. Dyn. Behav. Mater. 2 (2016) 43–49, https://doi.org/10.1007/s40870-015-0042-2.
[57] S.E. Rigby, A. Tyas, S.D. Clarke, S.D. Fay, J.J. Reay, J.A. Warren, M. Gant, I. Elgy, Observations from preliminary experiments on spatial and temporal pressure measurements from near-field free air explosions, Int. J. Prot. Struct. 6 (2015) 175–190.
[58] A.D. Barr, S.E. Rigby, S.D. Clarke, D. Farrimond, A. Tyas, Temporally and spatially resolved reflected overpressure measurements in the extreme near field, Sensors 23 (2023) 964.
[59] S. Clarke, S. Rigby, S. Fay, A. Barr, A. Tyas, M. Gant, I. Elgy, Characterisation of buried blast loading, Proc. R. Soc. A 476 (2020) 20190791.
[60] S.E. Rigby, R. Knighton, S.D. Clarke, A. Tyas, Reflected near-field blast pressure measurements using high speed video, Exp. Mech. 60 (2020) 875–888.
[61] S.E. Rigby, A. Tyas, T. Bennett, Elastic–plastic response of plates subjected to cleared blast loads, Int. J. Impact Eng. 66 (2014) 37–47, https://doi.org/10.1016/j.ijimpeng.2013.12.006.
[62] O. Al-Ketan, D.-W. Lee, R. Rowshan, R.K.A. Al-Rub, Functionally graded and multi-morphology sheet TPMS lattices: Design, manufacturing, and mechanical properties, J. Mech. Behav. Biomed. Mater. 102 (2020), 103520.
[63] R.H. Myers, D.C. Montgomery, C.M. Anderson-Cook, Response surface methodology: process and product optimization using designed experiments, John Wiley & Sons, 2016.
[64] R. Santiago, S. Almahri, D.-W. Lee, H. Alabdouli, O. Banabila, H. Ramos, M. Alteneiji, Z. Guan, M. Alves, Mechanical characterization and numerical modeling of TPMS lattice structures subjected to impact loading, : EPJ Web Conf., EDP Sci. (2021) 2005.
[65] R. Santiago, H. Ramos, S. AlMahri, O. Banabila, H. Alabdouli, D.-W. Lee, A. Aziz, N. Rajput, M. Alves, Z. Guan, Modelling and optimisation of TPMS-based lattices subjected to high strain-rate impact loadings, Int. J. Impact Eng. (2023), 104592.
[66] E. Tascioglu, Y. Karabulut, Y. Kaynak, Influence of heat treatment temperature on the microstructural, mechanical, and wear behavior of 316L stainless steel fabricated by laser powder bed additive manufacturing, Int. J. Adv. Manuf. Technol. 107 (2020) 1947–1956.
[67] I. Echeta, X. Feng, B. Dutton, R. Leach, S. Piano, Review of defects in lattice structures manufactured by powder bed fusion, Int. J. Adv. Manuf. Technol. 106 (2020) 2649–2668.
[68] N.B. Ghisi, H. Ramos, L. Kindleyside, N.T. Aboulkhair, R. Santiago, The influence of the characteristic microstructure of additively manufactured AlSi10Mg on the plastic behaviour at various strain rates, Mater. Des. 223 (2022), 111112.
[69] A.G. Hanssen, L. Olovsson, R. Porcaro, M. Langseth, A large-scale finite element point-connector model for self-piercing rivet connections, Eur. J. Mech. - A/Solids 29 (2010) 484–495, https://doi.org/10.1016/j.euromechsol.2010.02.010.
[70] J.K. Sønstabø, D. Morin, M. Langseth, Static and dynamic testing and modelling of aluminium joints with flow-drill screw connections, Int. J. Impact Eng. 115 (2018) 58–75, https://doi.org/10.1016/j.ijimpeng.2018.01.008.
[71] B. Zhang, Y. Li, Q. Bai, Defect formation mechanisms in selective laser melting: a review, Chin. J. Mech. Eng. 30 (2017) 515–527.
[72] L. Chen, Z. Liu, P. Sun, W. Huo, Formulation of a fuel spray SMD model at atmospheric pressure using Design of Experiments (DoE, Fuel 153 (2015) 355–360, https://doi.org/10.1016/j.fuel.2015.03.013.
[73] V.S. Deshpande, M.F. Ashby, N.A. Fleck, Foam topology: Bending versus stretching dominated architectures, Acta Mater. 49 (2001) 1035–1040, https://doi.org/10.1016/S1359-6454(00)00379-7.
[74] L.J. Gibson, M.F. Ashby, Cellular Solids, Cambridge University Press, 1997, https://doi.org/10.1017/CBO9781139878326.
[75] S. Li, M. Hu, L. Xiao, W. Song, Compressive properties and collapse behavior of additively-manufactured layered-hybrid lattice structures under static and dynamic loadings, Thin-Walled Struct. 157 (2020), 107153.
[76] C. Ling, A. Cernicchi, M.D. Gilchrist, P. Cardiff, Mechanical behaviour of additively-manufactured polymeric octet-truss lattice structures under quasi-static and dynamic compressive loading, Mater. Des. 162 (2019) 106–118, https://doi.org/10.1016/j.matdes.2018.11.035.
[77] J. Plocher, A. Panesar, Effect of density and unit cell size grading on the stiffness and energy absorption of short fibre-reinforced functionally graded lattice structures, Addit. Manuf. 33 (2020), 101171, https://doi.org/10.1016/j.addma.2020.101171.
[78] H. Shi-sheng, W. Li-li, S. Li, Z. Lei, Review of the development of Hopkinson pressure bar technique in China, 爆炸与冲击 34 (2014) 641–657.
[79] M.A. Kariem, R.C. Santiago, R. Govender, D.W. Shu, D. Ruan, G. Nurick, M. Alves, G. Lu, G.S. Langdon, Round-Robin test of split Hopkinson pressure bar, Int. J. Impact Eng. 126 (2019) 62–75, https://doi.org/10.1016/j.ijimpeng.2018.12.003.